Preprint typeset using LaTeX style emulateapj v. 05/04/06

FORMATION AND EVOLUTION OF GALAXY DARK MATTER HALOS AND THEIR SUBSTRUCTURE

Jürg Diemand[1,2], Michael Kuhlen[3], & Piero Madau[1,4]

ABSTRACT

We use the "Via Lactea" simulation to study the co-evolution of a Milky Way-size ΛCDM halo and its subhalo population. While most of the host halo mass is accreted over the first 6 Gyr in a series of major mergers, the physical mass distribution [not $M_{\rm vir}(z)$] remains practically constant since $z = 1$. The same is true in a large sample of ΛCDM galaxy halos. Subhalo mass loss peaks between the turnaround and virialization epochs of a given mass shell, and declines afterwards. 97% of the $z = 1$ subhalos have a surviving bound remnant at the present epoch. The retained mass fraction is larger for initially lighter subhalos: satellites with maximum circular velocities $V_{\rm max} = 10$ km/s at $z = 1$ have today about 40% of their mass back then. At the first pericenter passage a larger average mass fraction is lost than during each following orbit. Tides remove mass in substructure from the outside in, leading to higher concentrations compared to field halos of the same mass. This effect, combined with the earlier formation epoch of the inner satellites, results in strongly increasing subhalo concentrations towards the Galactic center. We present individual evolutionary tracks and present-day properties of the likely hosts of the dwarf satellites around the Milky Way. The formation histories of "field halos" that lie today beyond the Via Lactea host are found to strongly depend on the density of their environment. This is caused by tidal mass loss that affects many field halos on eccentric orbits.

Subject headings: cosmology: theory – dark matter – galaxies: dwarfs – galaxies: formation – galaxies: halos – methods: numerical

1. INTRODUCTION

Cosmological N-body simulations with large dynamic range (i.e. with large numbers of particles per virialized object and adequately high force and time resolution) make it possible to follow the highly non-linear formation of cold dark matter (CDM) halos and their substructure in great detail (e.g. Ghigna et al. 1998, 2000; Klypin et al. 1999; Moore et al. 1999, 2001; Fukushige et al. 2004; Kravtsov et al. 2004; Diemand et al. 2004; Gao et al. 2004; Gill et al. 2005; Reed et al. 2005). We have recently completed "Via Lactea", the highest resolution simulation to date of CDM substructure. The run was completed in 320,000 CPU hours on NASA's Project Columbia supercomputer, and follows the formation of a Milky Way-size halo with 234 million particles, an order of magnitude more than achieved previously. The present-day properties of the galaxy host and its substructure were presented in Diemand, Kuhlen, & Madau (2007, hereafter Paper I). In this second paper we use data extracted from all 200 snapshots stored during the Via Lactea run to study the mass assembly history of the main halo and the subhalo population.

Ghigna et al. (1998) and Bullock et al. (2001) have noted that subhalos are more concentrated than field halos. We now have the resolution and statistics to quantify this effect, and the large number of snapshots allows us to understand its origin. We can follow the evolution of massive subhalos at similar or higher resolution as in idealized N-body experiments that evolve one satellite in an external potential (e.g. Hayashi et al. 2003; Dekel et al. 2003; Kazantzidis et al. 2004; Read et al. 2006), but within a "live" host halo forming and evolving within the cosmological context. The increased resolution allows more accurate estimates of the fraction of subhalos that survive, the mass they retain, the effect of tidal stripping on their internal structure. How subhalo density profile and concentrations evolve during tidal mass loss? Are subhalos really fully disrupted once the tidal radius at pericenter is smaller than their scale radius (Hayashi et al. 2003)? How strongly does the heating from tidal shocks reduce inner subhalo densities? Or do tides in the inner, shallow part of the host lead to subhalo compression (Dekel et al. 2003)?

One interesting result that becomes apparent in cosmological simulations when tracking halos moving within a cluster potential is that many (sub)halos that were well within the cluster virial radius $r_{\rm vir}$ at some earlier time can be found today beyond $r_{\rm vir}$ (Balogh et al. 2000; Moore et al. 2004; Gill et al. 2005). This implies that the formation histories of "field" galaxy halos are affected by their environment, as many of the halos found in the outskirts of larger systems today may have shed mass during an earlier pericenter passage because of tidal interactions. Significant correlations between the formation times of galaxy-size halos of a fixed mass, their clustering strength (Sheth & Tormen 2004; Gao et al. 2005), and the density of their environment (Harker et al. 2006) have indeed been found. In this work, we show that these correlations are caused by tidal interactions of (sub)halos on extended radial orbits with a more massive neighbor.

This paper is organized as follows. In § 2 we study the mass assembly of the Via Lactea host and its substructure population, and introduce physical (non-comoving) general definitions of (sub)halo properties like size, mass,

[1] Department of Astronomy & Astrophysics, University of California, Santa Cruz, CA 95064.
[2] Hubble Fellow.
[3] School of Natural Sciences, Institute for Advanced Study, Einstein Drive, Princeton, NJ 08540.
[4] Max-Planck-Institut für Astrophysik, Karl-Schwarzschild-Str. 1, 85740 Garching, Germany.
email: diemand@ucolick.org, mqk@ias.edu, pmadau@ucolick.org.

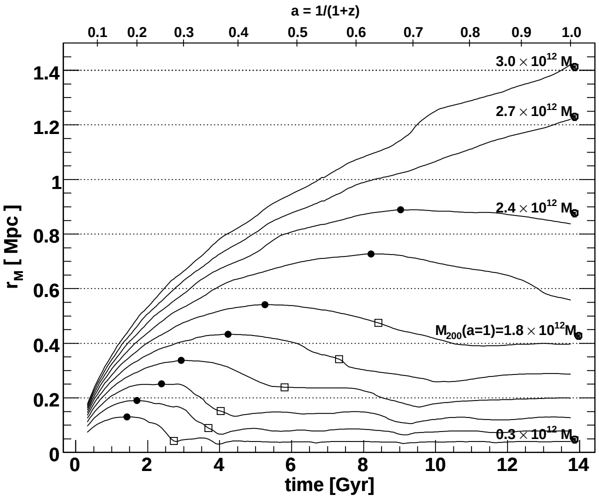

FIG. 1.— Evolution of radii r_M enclosing a fixed mass versus cosmic time or scale factor a. The enclosed mass grows in constant amounts of 0.3×10^{12} $M_\odot$ from bottom to top. Shells are numbered from one (inner) to ten (outer). Initially all spheres are growing in the physical (non comoving) units used here. Shells 1 to 6 turn around, collapse and stabilize, while the outermost shells are still expanding today. *Solid circles*: points of maximum expansion at the turnaround time $t_{\rm ta}$. *Open squares:* time after turnaround where $r_{\rm M}$ first contracts within 20% of the final value. These mark the approximate epoch of stabilization. The collapse factors $r_M(t_{\rm ta})/r_M(z=0)$ for shells 1 to 6 are 3.29, 2.44, 1.98, 1.70, 1.51 and 1.36, respectively. Thus shells 1 and 2 collapse by more than the factor of 2 derived from spherical top-hat, while shells 4, 5, and 6 collapse by a smaller factor.

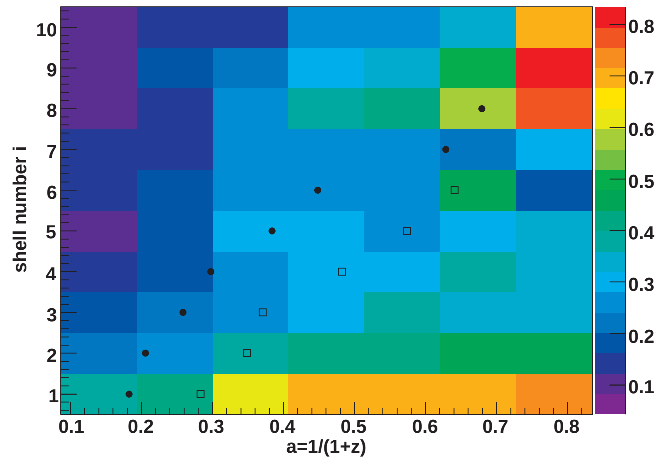

FIG. 2.— Fraction of material belonging to shell i at epoch a that remains in the same shell today. Shells are same as in Fig. 1, numbered from one (inner) to ten (outer). *Solid circles*: time of maximum expansion. *Open squares:* stabilization epoch. Mass mixing generally decreases with time and towards the halo center.

concentration, and formation time. Section 3 discusses the evolution of subhalo concentrations and abundance in fixed-mass shells around the host. In § 4 we analyze individual and ensemble-averaged evolutionary tracks of subhalos and discuss how their density profiles evolve during tidal shocks at pericenter. We present the histories and present-day properties of the likely hosts of the dwarf satellites around the Milky Way. Average histories of subhalos found in certain regions today and their survival from $z = 1$ to $z = 0$ are also discussed in this section. Finally, § 5 summarizes our conclusions.

2. FORMATION HISTORIES OF GALAXY HALOS

The Via Lactea simulation was performed with the PKDGRAV tree-code (Stadel 2001) and employed multiple mass particle grid initial conditions generated with the GRAFICS2 package (Bertschinger 2001). The high resolution region was sampled with 234 million particles particles of mass $2.1 \times 10^4\,{\rm M}_\odot$ and evolved with a force resolution of 90 pc. It was embedded within a periodic box of comoving size 90 Mpc, which was sampled at lower resolution to account for the large scale tidal forces. We adopted the best-fit cosmological parameters from the *WMAP* 3-year data release (Spergel et al. 2006): $\Omega_M = 0.238$, $\Omega_\Lambda = 0.762$, $H_0 = 73\,{\rm km\,s^{-1}\,Mpc^{-1}}$, $n = 0.951$, and $\sigma_8 = 0.74$. The simulation was centered on an isolated halo that had no major merger after $z = 1.7$, which makes it plausible that this halo would be a suitable host for a Milky Way-like disk galaxy (e.g. Governato et al. 2007). More details about the Via Lactea run are given in Paper I. Movies, images, and data are available at http://www.ucolick.org/∼diemand/vl. The host halo mass at $z = 0$ is $M_{200} = 1.77 \times 10^{12}$ $M_\odot$ within a radius of $r_{200} = 389$ kpc (we define r_{200} as the radius within which the enclosed average density is 200 times the mean matter density $\Omega_M\,\rho_{\rm crit}$. Note that M_{200} and r_{200} were denoted in Paper I as $r_{\rm vir}$ and $M_{\rm halo}$. We revert here to the more standard notation for reasons of clarity.).

Before describing the evolution of substructure, we have to address the following issues. When does a halo become a subhalo? When does the host form and how does it grow? Which regions/volumes should be used for a meaningful comparison of subhalo abundances and average properties at different cosmic epochs? The common procedure is to define at each epoch a "virial" radius $r_{\rm vir}$, which depends on the cosmic background density at the time, and define subhalos as bound clumps within this volume. These definitions are not ideal for two reasons. First, halos cross this artificial boundary not only inward ("accretion") but about as often also outwards. Averaging over six, relaxed galaxy clusters, no net infall of subhalos into the virial region was found in Diemand et al. (2004), and half of the halos found today between $r_{\rm vir}$ and $2\,r_{\rm vir}$ had actually passed through the cluster at some earlier time (Balogh et al. 2000; Moore et al. 2004; Gill et al. 2005). Macciò et al. (2003) noted that the virialized regions of halos are often larger than $r_{\rm vir}$, and a lack of mass infall out to 2-3 virial radii was found for a large, representative sample of galaxy halos by Prada et al. (2006). This leads directly to the second problem. As the cosmic background density decreases with Hubble expansion, formal virial radii and masses grow with cosmic time even for stationary halos. Studying the transformation of halo properties within $r_{\rm vir}$ (or some fraction of it) mixes real physical change with apparent evolutionary effects caused by the growing radial window, and makes it hard to disentangle between the two.

To address the second problem, we describe here the formation of Via Lactea using radial shells enclosing a fixed mass, $r_{\rm M}$. Unlike $r_{\rm vir}$, $r_{\rm M}$ stops growing as soon as the mass distribution of the host halo becomes stationary on the corresponding scale (see Fig. 1). The first problem, however, remains. Mass and substructure are constantly exchanged between these shells, as $r_{\rm M}$ is

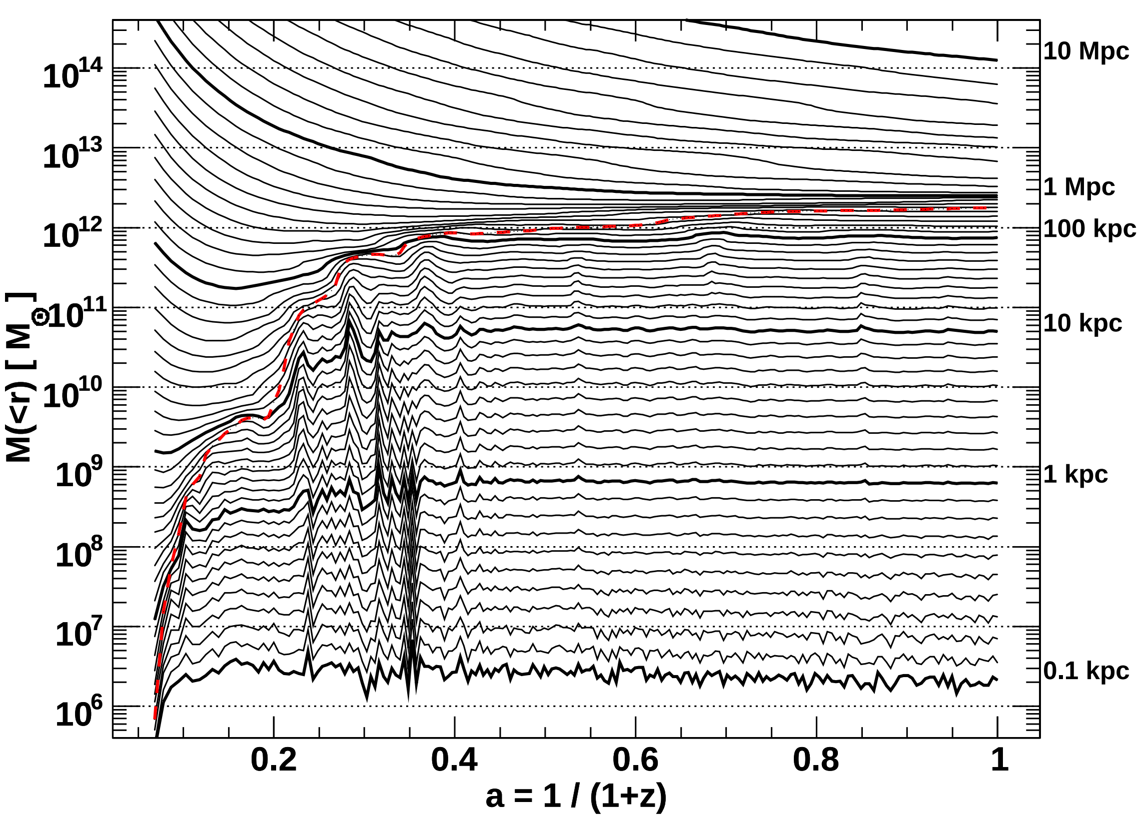

Fig. 3.— Mass accretion history of Via Lactea. Masses within spheres of fixed physical radii centered on the main progenitor are plotted against the cosmological expansion factor a. The thick solid lines correspond to spheres with radii given by the labels on the right. The thin solid lines correspond to nine spheres of intermediate radii that are 1.3, 1.6, 2.0, 2.5, 3.2, 4.0, 5.0, 6.3 and 7.9 times larger than the next smaller labeled radius. *Dashed line:* M_{200}. The halo is assembled during a phase of active merging before $a \simeq 0.37$ ($z \simeq 1.7$) and remains practically stationary at later times.

not a Lagrangian radius enclosing the same material at all times, just the same amount of it. The fraction of material belonging to a given shell in the past that still remains within the same shell today is shown in Figure 2. The mixing is larger before stabilization, presumably because of shell crossing during collapse. In the stationary phase the shells still exchange mass because many particles are on radial orbits. The mixing is smaller near the halo center, where most of the mass is in a dynamically cold, concentrated component that originated from the earliest forming high-σ progenitors (Diemand et al. 2005).

2.1. *Collapse times and collapse factors*

In spherical top-hat collapse, a shell has no kinetic energy at turnaround and virializes at half the turnaround radius. The final overdensity relative to the critical density at the collapse redshift is $\Delta = 18\pi^2$ in the Einstein-de Sitter model, modified in a flat Universe with a cosmological constant to the fitting formula (Bryan & Norman 1998)

$$\Delta = 18\pi^2 - 82\Omega_\Lambda(z) - 39\Omega_\Lambda^2(z), \qquad (1)$$

where

$$\Omega_\Lambda(z) = \frac{\Omega_\Lambda}{\Omega_m(1+z)^3 + \Omega_\Lambda}. \qquad (2)$$

At $z = 0$ and for a *WMAP* 3-year cosmology, this yields $\Delta = 93$. Here we introduce the modified formula,

$$\Delta = 200 - 82\Omega_\Lambda(z) - 39\Omega_\Lambda^2(z), \qquad (3)$$

and define the virial radius $r_{\rm vir}$ as the radius enclosing a mean density $\Delta\rho_{\rm crit}$. At $z = 0$ this yields $\Delta = 104$ and $r_{\rm vir} = 288$ kpc for Via Lactea. We chose this slightly different definition for the collapse overdensity so that, at high redshifts, $r_{\rm vir}$ approaches r_{200}.

The simple spherical top-hat collapse ignores shell crossing and mixing, triaxiality, angular momentum, random velocities, and large scale tidal forces. Figure 1 shows that spheres enclosing a fixed mass have collapse factors that differ from 2. Inner shells collapse by larger factors, in qualitative agreement with the modified spherical collapse model of Sanchez-Conde et al. (2006) that accounts for shell crossing but not angular momentum. Shells enclosing about the standard viral mass collapse by less than a factor of 2, probably because of the significant kinetic energy they contain already at turnaround. The collapse times are also different from spherical top-hat. Shell number five, for example, encloses a mean density of about $104\,\rho_{\rm crit}$ today, a virial mass of 1.5×10^{12} M$_\odot$ and should have virialized just now according to spherical top-hat. It did so instead much earlier, at $a = 0.6$. Even the next larger shell with 1.8×10^{12} M$_\odot$ stabilized before $a = 0.8$. Our analysis supports the point made by Prada et al. (2006), that spherical top-hat provides only a crude approximation to the virialized regions of simulated galaxy halos.

2.2. *Accretion histories*

To understand the mass accretion history of the Via Lactea halo we now analyze the evolution of mass within fixed physical radii. Figure 3 shows that the mass within all radii from the resolution limit of $\simeq$1 kpc up to 100 kpc grows during a series of major mergers before $a = 0.4$. After this phase of active merging and mass accretion the entire system is almost perfectly stationary at all radii. The small decrease in density on scales below 1 kpc is likely an artifact of time-steps which are too large compared to the short dynamical time in these inner regions (Paper I). A similar decrease in density in the inner regions of halos was shown to be caused by too large time steps in the convergence tests of Fukushige et al (2004; see their Figure 9). Only the outer regions ($\sim$ 400 kpc) experience a small amount of mass accretion after the last major merger, better visible in the linear mass scale of Figure 4. The mass within 400 kpc increases only mildly, by a factor of 1.2 from $z = 1$ to the present. During the same time the mass within radii of 100 kpc and smaller, the peak circular velocity, $V_{\rm max}$, and the radius where it is reached, $r_{\rm Vmax}$, all remain constant to within 10%. The lack of evolution in the inner density profile, and therefore also in $V_{\rm max}$, $r_{\rm Vmax}$ and $\rho(< r_{\rm Vmax})$, during this major merger-free phase agrees with the findings of previous studies (e.g. Wechsler et al. 2002; Zhao et al. 2003; Romano-Diaz et al. 2006).

The physical assembly of galaxy halos thus appears to occur mainly during an active early phase of major mergers, in which the halo peak circular velocity (and the enclosed mass at all radii) grows to its maximum value. In contrast to previous work on this subject (Wechsler et al. 2002; Zhao et al. 2003), we do not find evidence for much mass growth during the late "slow accretion" phase, *when the definition of halo mass is based on physical instead of comoving scales*. Rather, the mass distribution and peak circular velocity appear to remain constant for the majority of the halo's lifetime. The fact that mass definitions inspired by spherical top-hat fail to accurately describe the real assembly of galaxy halos is clearly seen in Figure 4, where M_{200} and $M_{\rm vir}$ are shown to increase even when the halo physical mass remains the same. This is just an artificial effect caused by the growing radial windows $r_{\rm vir}$ and r_{200} as the background density decreases. For Via Lactea M_{200} increases by a factor of 1.8 from $z = 1$ to the present, while the real physical mass within a 400 kpc sphere grows by only a factor of 1.2 during the same time interval, and by an even smaller factor at smaller radii.

We find that the small physical accretion since $z = 1$ seen in Via Lactea is indeed typical of galaxy halos. In a 45 Mpc periodic box resolved with 300^3 particles of mass $1.2 \times 10^8\,{\rm M}_\odot$ (simulated in a 3-year *WMAP* cosmology), we have identified 303 galaxy halos at $z = 0$ with M_{200} ranging from $0.6 \times 10^{12}\,{\rm M}_\odot$ to $5.4 \times 10^{12}\,{\rm M}_\odot$. The mass within a constant physical radius of 400 kpc grows by a factor of $1.15^{+0.39}_{-0.16}$ (the errors indicate the 68% range around the median) since $z = 1$ ("physical accretion"), whereas M_{200} grows by a factor of $2.10^{+1.17}_{-0.59}$ ("apparent accretion"). For lower mass halos the physical accretion is even smaller. In the same 45 Mpc box we find 714 halos with M_{200} ranging from $1.5 \times 10^{11}\,{\rm M}_\odot$ to $4.5 \times 10^{11}\,{\rm M}_\odot$ today. From $z = 1$ to the present their mass within 200 kpc ($\sim r_{200}$ at $z = 0$) grows by a factor of only $1.12^{+0.26}_{-0.17}$, whereas M_{200} increases by $1.85^{+0.96}_{-0.40}$. Physical and apparent accretion are correlated, but with a large scatter.

Within the inner 20 kpc, i.e. where the galaxy is expected to lie, the gravitational potential remains constant during the late, quiescent phases of halo formation (Figure 3). Unless there is an evolving, dominant baryonic mass contribution, the rotation rate of the galactic disk should not evolve in time, with a peak circular velocity that may be proportional to the constant peak circular velocity of its halo. Assumptions sometimes made in semi-analytic models about evolution of galaxy properties with halo virial quantities (e.g. stellar mass with $M_{\rm vir}$) will produce inaccurate results, considering the different length scales and the lack of physical accretion both on small and large scales. Models based on quantities that do remain constant during stationary phases, like peak circular velocity and the corresponding radius and enclosed mass, may be more physical. Observations of representative samples of $z = 1$ galaxies, including kinematics, are now becoming available (e.g. Weiner et al. 2006; Kassin et al. 2007) and it might be possible to test whether galaxy radii and masses grow like the halo virial scales (i.e. by about a factor of two) or if they remain constant like the halo mass distribution on physical scales.

2.3. *Formation times*

As discussed above, the common spherical top-hat inspired halo mass definitions M_{200} and $M_{\rm vir}$ are not well suited to describe the growth of galaxy halos. Care should also be used when the complex and extended process of halo formation is quantified with a single number, the so called "halo formation time". Many of the existing definitions are based on the evolution of M_{200} or $M_{\rm vir}$ (e.g. Wechsler et al. 2002; Zhao et al. 2003; Gao et al. 2005). For galaxy halos such formation times depend almost exclusively on the amount of apparent accretion [5], which dominates the evolution of M_{200} and $M_{\rm vir}$ for more than half of the age of the universe and, in many cases, contributes more than half of the total "accreted" mass. Since apparent accretion correlates only weakly with physical halo growth, it is unclear how and if halo formation times calculated in this manner do relate to the epoch when most of the physical halo assembly took place. Our analysis also casts doubt on whether such formation times are at all related to the relevant timescales for galaxy formation.

Consider, as an example, the widely used definition of formation time as the time when M_{200} (or similarly the FOF mass based on a comoving linking length of 0.2 times the mean particle separations) reaches half of the present value. More than half of our large, low-resolution sample of galaxy-size halos would form after $z = 1$ according to this definition, yet their physical mass accretion is less than 20% over this time span; *their mass*

[5] The amount of apparent accretion depends on how much mass lies in the outer halo, i.e. it is larger for halos with low concentrations.

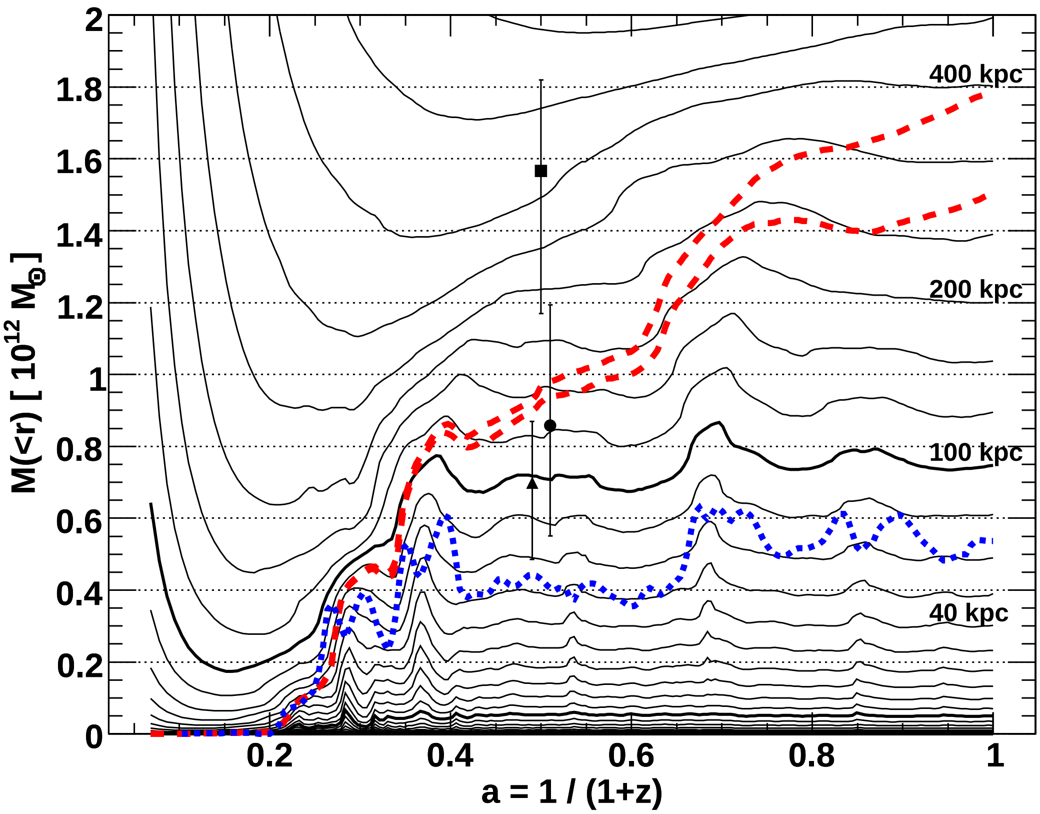

FIG. 4.— Same as Figure 3, but using a linear scale in enclosed mass. In addition to M_{200} (*upper dashed line*) we now also plot $M_{\rm vir}$ (*lower dashed line*) and the mass within the radius of maximal circular velocity (*dotted line*). The physical mass accretion is small after the last major merger at $a \simeq 0.37$ ($z \simeq 1.7$): more than 80% of the present-day material within 400 kpc is already in place at $z = 1$. This value is typical for galaxy-size halos. *Filled square:* median $z = 1$ mass fraction (= 0.87) within 400 kpc for 303 halos of similar mass rescaled to today's Via Lactea mass within 400 kpc. *Solid circle*: corresponding median $z = 1$ value for M_{200}. *Filled triangle:* corresponding median $z = 1$ value for the mass within 100 kpc. Error bars indicate the 68% scatter around the median.

assembly was practically completed before their formal "formation time". The Via Lactea halo would have a formation redshift of $z \simeq 1$ according to this definition (see Figure 4), which is also well after the epoch when most of the physical mass accretion actually took place. To address this issue, we propose a formation time based on peak circular velocity, a quantity that does not evolve during the stationary phase of a halo. We define the halo formation epoch $z_{\rm form}$ to be equal to the earliest time when $V_{\rm max}$ reaches 85% of its highest value at all redshifts:

$$V_{\rm max}(z_{\rm form}) \equiv 0.85 \ \max_z\{V_{\rm max}(z)\} \ . \qquad (4)$$

Note that a definition of formation time based on the present-day peak circular velocity $V_{\rm max}(z = 0)$ would lead to significantly higher median formation redshifts, since for many halos $V_{\rm max}$ is reduced by tidal stripping. We will show in Section 4.4 that this is true even for halos beyond the virial radius today, i.e. for "field" halos. For comparison, we define the redshift z_{85} as

$$V_{\rm max}(z_{85}) \equiv 0.85 \ V_{\rm max}(z = 0) \ , \qquad (5)$$

but throughout this work we mean $z_{\rm form}$ (eq. 4) when we refer to a halo formation time. In Section 4.4 we will find a clear environmental dependence in the median z_{85} of field halos, but not in their median $z_{\rm form}$.

2.4. *A physical (sub)halo concentration index: c_V*

Often halo concentrations are presented in terms of the virial concentration index defined as the ratio $c_{\rm vir} = r_{\rm vir}/r_s$, where r_s is the scale radius of an NFW fit (e.g. Navarro et al. 1997; Bullock et al. 2001; Wechsler et al. 2002; Kuhlen et al. 2005; Maccio' et al. 2006). This definition has two drawbacks: 1) $c_{\rm vir}$ grows even during epochs of "apparent accretion", when the physical mass distribution remains constant. In Via Lactea, for example, the mass distribution remains nearly unchanged from $z = 1$ to $z = 0$, but $c_{\rm vir}$ grows by about a factor of two because of the comoving definition of $r_{\rm vir}$; and 2) subhalos are truncated at the tidal radius, which is always smaller than their formal virial radius, i.e. virial radii and thus $c_{\rm vir}$ are not well defined for subhalos.

A direct measure of physical density in the inner regions of halos is provided by the "central density parameter" $\Delta_{V/2}$, introduced by Alam et al. (2002). Here we refer to this parameter as c_V, to avoid confusion with the virial overdensity Δ.

$$c_{V/2} \equiv \frac{\bar{\rho}(< r_{\rm Vmax/2})}{\rho_{\rm crit,0}} = \frac{1}{2}\left(\frac{V_{\rm max}}{H_0 r_{\rm Vmax/2}}\right)^2 , \qquad (6)$$

where $r_{\rm Vmax/2}$ is the radius at which the circular velocity curve reaches half its maximum value. With this definition $c_{\rm V/2}\rho_{\rm crit,0}$ is equal to the mean physical den-

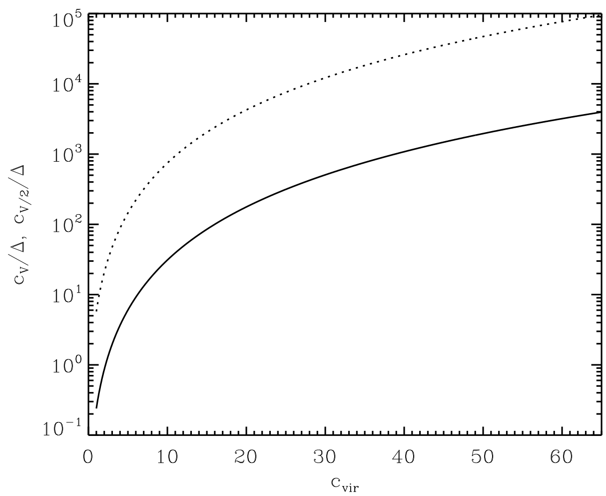

FIG. 5.— Concentration parameters c_V (*solid*) and $c_{V/2}$ (*dotted*) divided by the density contrast Δ used to define $r_{\rm vir}$ at $z = 0$, as a function of $c_{\rm vir} = r_{\rm vir}/r_s$.

sity within $r_{\rm Vmax/2}$ and has the advantage that it can be directly measured in numerically simulated dark matter halos and in observed galactic rotation curves, *without reference to any particular analytic density profile*. Unfortunately, even with Via Lactea's extreme resolution, an accurate determination of $r_{\rm Vmax/2}$ is not possible for all but the most massive subhalos. Since $r_{\rm Vmax}$ is better measured, however, we use instead c_V, the mean physical density within the radius of the peak circular velocity in units of $\rho_{\rm crit,0}$, as our new physical concentration parameter:

$$c_V \equiv \frac{\bar{\rho}(< r_{\rm Vmax})}{\rho_{\rm crit,0}} = 2\left(\frac{V_{\rm max}}{H_0 r_{\rm Vmax}}\right)^2. \qquad (7)$$

For any given analytic density profile it is straightforward to convert between $c_{\rm vir}$ and c_V. For an NFW (Navarro et al. 1997) density profile,

$$\rho(r) = \frac{\rho_s}{r/r_s(1+r/r_s)^2}, \qquad (8)$$

the circular velocity is

$$V_c(r) = 4\pi G\rho_s r_s^3 \frac{f(r)}{r}, \quad \textit{with} \qquad (9)$$

$$f(r) = \ln(1+r/r_s) - \frac{r/r_s}{1+r/r_s}. \qquad (10)$$

The maximum of $V_c(r)$ occurs at

$$r_{\rm Vmax} = 2.163\, r_s. \qquad (11)$$

The NFW scale density ρ_s can be expressed in terms of the concentration $c_{\rm vir}$ and the spherical top-hat virial density contrast Δ (cf. Section 2.1)

$$\rho_s = \frac{1}{3}\frac{c_{\rm vir}^3}{f(r_{\rm vir})}\Delta(z)\rho_{\rm crit}(z). \qquad (12)$$

Combining eqs. (9), (11), and (12), we find

$$c_V = \left(\frac{c_{\rm vir}}{2.163}\right)^3 \frac{f(r_{\rm Vmax})}{f(r_{\rm vir})}\Delta(z)\,\frac{\rho_{\rm crit}(z)}{\rho_{\rm crit,0}}. \qquad (13)$$

Figure 5 shows a plot of c_V divided by the density contrast Δ used to define $r_{\rm vir}$ and $c_{\rm vir}$, as a function of $c_{\rm vir}$. For comparison, we also show $c_{V/2}/\Delta$. Note that c_V is defined in terms of $\rho_{\rm crit}$ today, whereas $c_{\rm vir}$ explicitely depends on redshift through $\Delta(z)$ and $\rho_{\rm crit}(z)$. The values of c_V for a given $c_{\rm vir}$ that can be read off from Figure 5 are thus only valid at $z = 0$; at higher redshifts they must be multiplied by $[\Delta(z)\rho_{\rm crit}(z)]/[\Delta(0)\rho_{\rm crit,0}]$. At $z = 0$ the Via Lactea host halo has a concentration of $c_V = 3613$, which corresponds to $c_{\rm vir} = 10.4$. This compares well with the value of $c_{\rm vir} = 11.7$ determined from the best fitting NFW model.

3. EVOLUTION OF SUBHALO PROPERTIES

The present-day cumulative subhalo mass function within Via Lactea is well approximated by a simple power law

$$N(> M_{\rm sub}) = 0.0064\left(\frac{M_{\rm sub}}{M_{200}}\right)^{-\alpha_M}, \qquad (14)$$

with slope[6] $\alpha_M \simeq 1$ and host halo mass $M_{200} = 1.8 \times 10^{12}\,{\rm M}_\odot$ (Paper I). Here $M_{\rm sub}$ is defined as the mass within the tidal radius $r_t \equiv r\sigma_{\rm sub}/(\sqrt{2}\sigma_{\rm host})$. This radius is the classical Jacobi limit for an isothermal satellite on a circular orbit of radius r within an isothermal host halo (see e.g. Read et al. 2006). It has the property that the host local density is half of the local satellite density at r_t. Similarly the $z = 0$ subhalo velocity function within r_{200} is fitted by

$$N(> V_{\rm max}) = 0.021\left(\frac{V_{\rm max}}{V_{\rm max,host}}\right)^{-\alpha_V}, \qquad (15)$$

with slope $\alpha_V \simeq 3$. Here we present the time evolution of the normalizations and slopes of these two power laws.

The large number of subhalos in Via Lactea allows us to study their abundance, distribution, and concentrations as a function of distance from the Galactic center. For this analysis we use the ten spherical shells plotted in Figure 1, each at all times containing a mass of $0.3 \times 10^{12}\,{\rm M}_\odot$ and centered on the main galaxy progenitor. Figure 6 shows the number of subhalos and the substructure mass fraction of each shell as a function of time. The amount of substructure is very closely linked to the formation history of its host: in each shell the number of subclumps peaks between the epochs of turnaround and stabilization. Some time after a shell has stabilized, the abundance of subhalos becomes nearly constant. Most of the tidal mass loss at a given radius happens early, during a relatively short epoch when the corresponding shell is near the end of its collapse and approaching stabilization, and most subhalos are experiencing their first pericenter passage (see §4.5). At low redshift, the mass in substructure lost from tidal effects or clumps orbiting out of the shell is approximately replaced by other clumps streaming into the shell. The number of satellites with $V_{\rm max} > 5$km/s within the final M_{200} (ie. within all six inner shells) remains within 25 % of its value at

[6] $N(> M_{\rm sub})$ is not a perfect power law: It becomes steeper at large masses, due to dynamical friction, and shallower at small masses, due to the gradually increasing importance of numerical resolution effects. Therefore the best fit slope depends on the mass range and the fitting procedure. For $M_{\rm sub} > 200\, m_p$ we find $\alpha_M = 0.97 \pm 0.03$. In the same mass range the differential mass function $dn(M_{\rm sub})/dM_{\rm sub}$ has $\alpha_{dM} = 1.90 \pm 0.02$. These best fit values differ by less than unity, because the differential mass function gives more weight to the relatively poorly resolved low mass end.

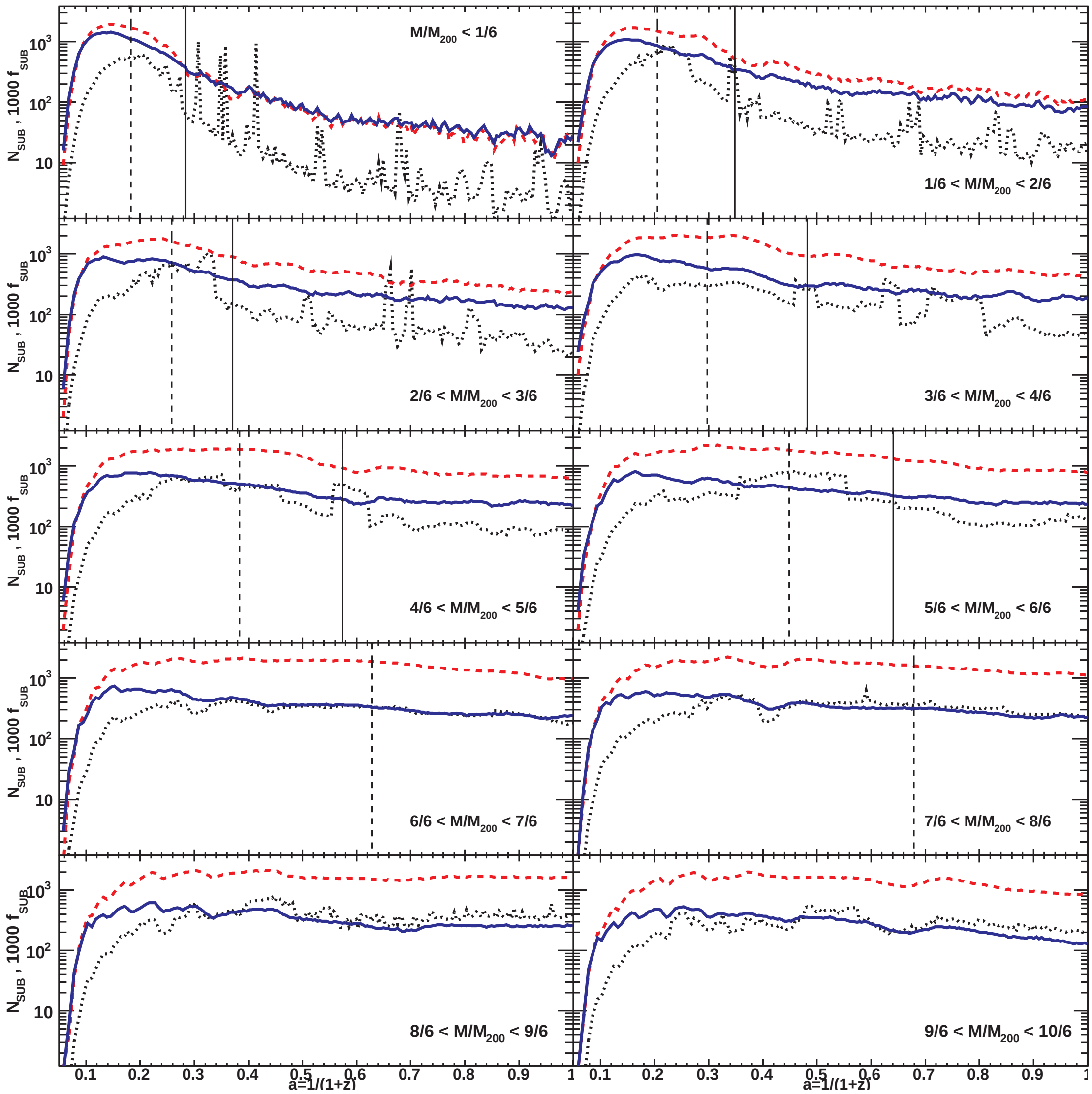

FIG. 6.— Abundance of (sub)halos versus time in shells containing a fixed mass and centered on the main Via Lactea progenitor at each time. Shells are ordered from inner (*top left*) to outer (*bottom right*). *Solid line:* number of subhalos with $V_{\rm max} > 5$ km/s.*Dashed line:* number of subhalos with $M_{\rm sub} > 4.0 \times 10^6\,{\rm M}_{\odot}$.*Dotted line:* mass fraction in resolved (sub)halos within each shell (excluding the most massive subhalo to avoid spikes as it orbits though the shells). The vertical dashed line marks the time of maximal expansion of the corresponding mass shell, and the vertical solid line the approximate stabilization epoch (see Figure 1). The subhalo mass loss rate peaks between these two epochs and declines after the region stabilizes.

$z = 0.5$ at all times until the present. This nearly constant substructure abundance over the last 5 Gyrs seems to be at odds with the recently found trends that old virialized systems are less clumpy (Gao et al. 2004; van den Bosch et al. 2005; Zentner et al. 2005). However, we too see such a trend for the larger subhalos: the number of subhalos with $V_{\rm max} > 10$ km/s within the final M_{200} decreases steadily from 159 at $z = 0.5$ to 112 at $z = 0$. It seems that the larger subhalos (roughly within three decades in mass of the host) are a transient population that declines continuously after the host has stabilized [7]. On smaller scales, however, substructure appears to be more persistent and less dependent of the age of the host (cf. Taffoni et al. (2003) and §4.6).

Today, the number of subhalos with $M_{\rm sub} > 4 \times 10^6\,{\rm M}_{\odot}$ is smaller in shells closer to the Galactic center, in agreement with previous studies (e.g. Ghigna et al. 2000; Diemand et al. 2004; Gao et al. 2004). The $z = 0$ number density of mass-selected subhalos is well described by a cored isothermal profiles with a scale radius similar to that of their host, as proposed by Diemand et al. (2004) and the ratio of subhalo number density and host matter density is simply proportional to radius:

$$\frac{n_{\rm M0}(r)}{\rho_{\rm host}(r)} \propto r \quad \text{for } 0.1 < r/r_{\rm vir} < 1.0\,. \tag{16}$$

This “spatial antibias” becomes smaller when subhalos are selected by their present $V_{\rm max}$, In this case the bias scales with enclosed host mass:

$$\frac{n_{V_{\rm max}0}(r)}{\rho_{\rm host}(r)} \propto M(<r) \quad \text{for } 0.1 < r/r_{\rm vir} < 1.0\,. \tag{17}$$

The velocity dispersions of these spatially extended samples are larger than the dispersions of the more concentrated, dark matter component, in good agreement

[7] Zentner et al. (2005) do indeed point out that this trend is stronger for more massive subhalos.

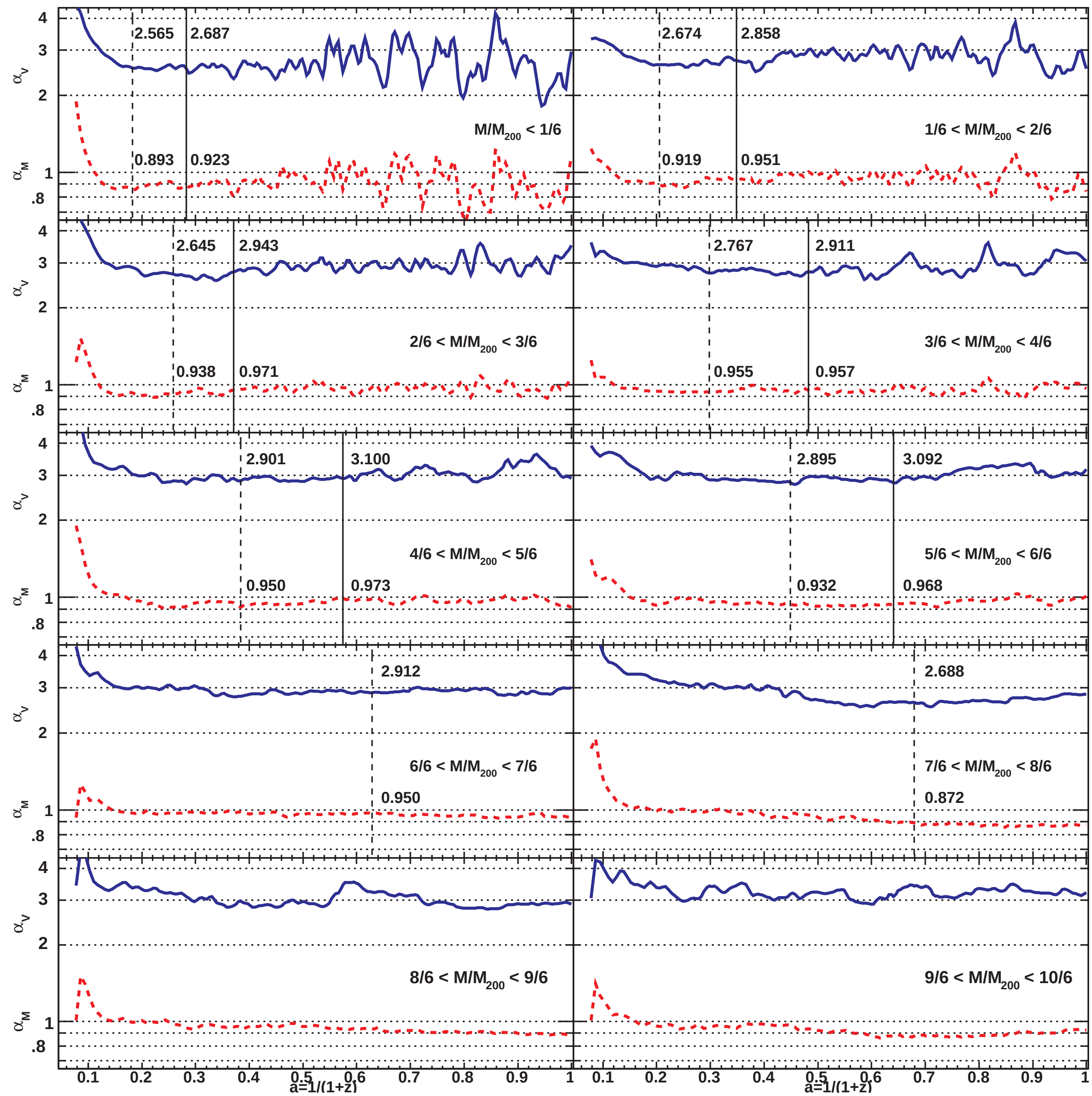

FIG. 7.— Evolution of the slopes of the cumulative subhalo velocity (*solid lines*) and mass (*dashed lines*) function in the same shells as in Fig. 6. Numbers depict the average slopes between the turnaround and stabilization epochs, and from stabilization to the present. The slopes show little trend with time or distance from the main progenitor.

with stationary solutions of the Jeans equation applied to this two component system (as in Diemand et al. 2004). The orbital anisotropy parameter $\beta = 1 - 0.5\sigma^2_{\rm tan}/\sigma^2_{\rm rad}$ is identical for both the subhalos and the dark matter: $\beta(r) \simeq 0.55(r/r_{\rm vir})^{1/3}$ for $0.2 < r/r_{\rm vir} < 1.0$. Tidal mass loss, which causes the spatial and velocity distributions of these subhalo samples to differ from the dark matter distribution, does not alter the orbital properties of substructure. Locally, we find a value of $\beta(r = 8\,{\rm kpc}) = 0.12$.

While today the distribution of satellites is more extended than the dark matter, the opposite is true at high redshifts: the inner shells are much more clumpy. At $a = 0.1$ even the smallest halos considered here ($4.0 \times 10^6\,{\rm M}_\odot$) correspond to rare density fluctuations (about 2σ). The enhanced subhalo abundance in inner shells at $a = 0.1$ thus reflects the bias of high-σ peaks towards the centers of larger scale fluctuations (Cole & Kaiser 1989; Sheth & Tormen 1999).

Figure 7 shows the best-fit power-law slopes of the substructure cumulative velocity function in the range $5 - 50$ km/s and the cumulative mass function in the range $4.0 \times 10^6 - 4.0 \times 10^9\ {\rm M}_\odot$. The innermost shell (top left) is affected by numerical resolution effects and small subhalo numbers. The slopes show no strong trends with time (as in Gao et al. 2004; Reed et al. 2005) or distance

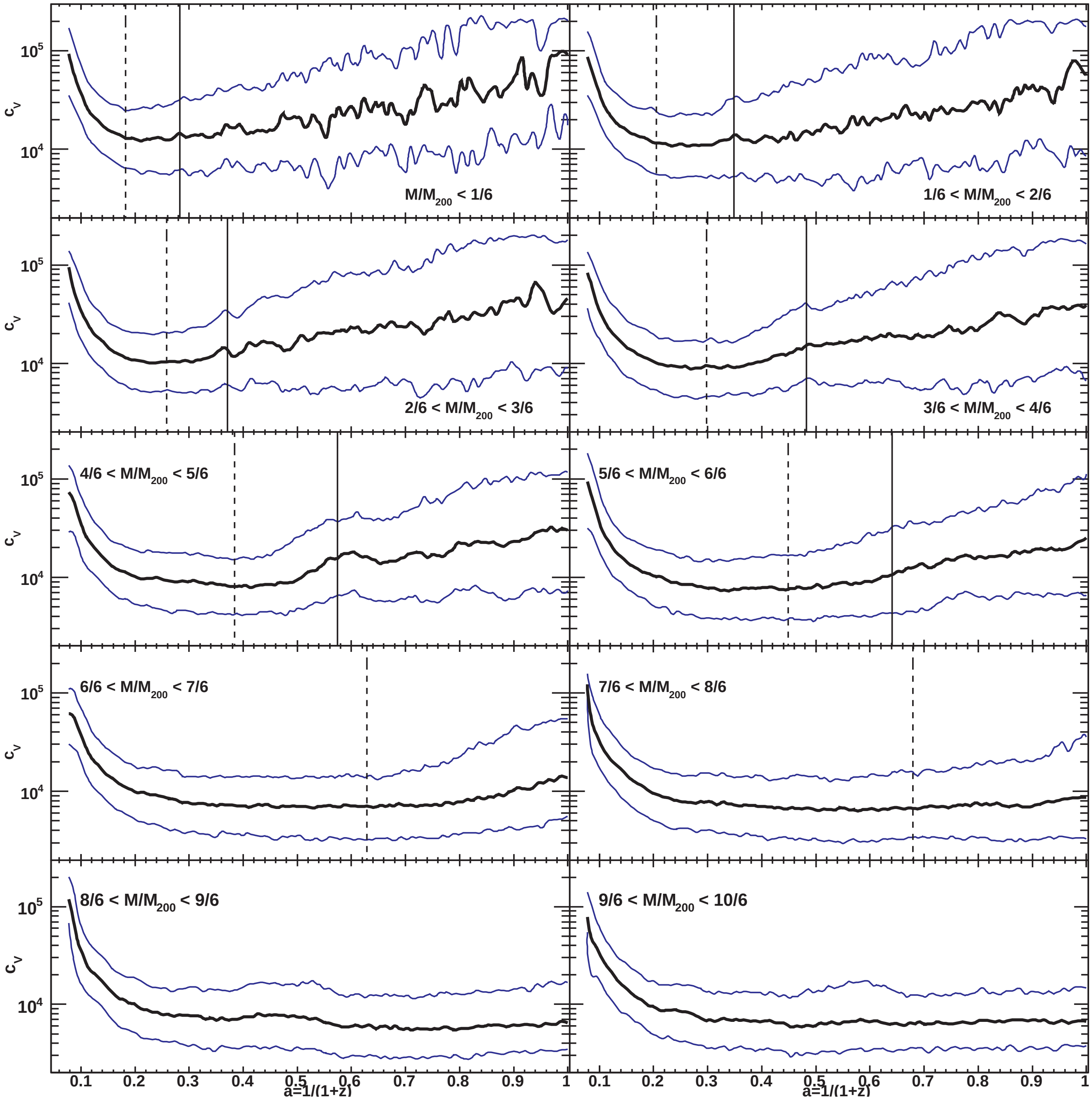

Fig. 8.— Same as Fig. 6, but now the evolution of the median subhalo concentration (*thick line*) is plotted versus scale factor. *Thin line:* 68% scatter around the median. All halos with $V_{\rm max} > 5$ km/s are included.

from the main progenitor. There is a slight trend toward steeper mass and velocity functions in the inner shells, and toward a steepening with time from the epoch between turnaround and stabilization. These small trends are suggestive of tidal mass losses being more significant in more massive systems and leading to steeper mass and velocity functions (see §4.6).

The evolution of the median concentration is shown in Figure 8. The concentration parameter is related to the cosmic mean density at the halo formation time (Navarro et al. 1997; Bullock et al. 2001; Wechsler et al. 2002). Early forming halos, which are well resolved in our simulation, do indeed have high concentrations in all radial shells.[8]. In the outer shell the median concentration decreases with time because of the continuous formation of new, lower concentration halos. In the inner shells the downward trend is halted as the shell collapses and the abundance of subhalos freezes (cf. Figure 6). Note how the level of this floor, between turnaround and stabilization of a shell, lies at higher concentrations for the inner shells as they turnaround at higher redshifts. After a shell stabilizes, the median concentration grows because tidal forces remove mass from the outer sub-

[8] With our physical (non-comoving) definition of concentration (eq. 7), early forming halos have high concentrations from the collapse redshift, whereas their $c_{\rm vir}$ parameter would grow with time to reach high values only recently.

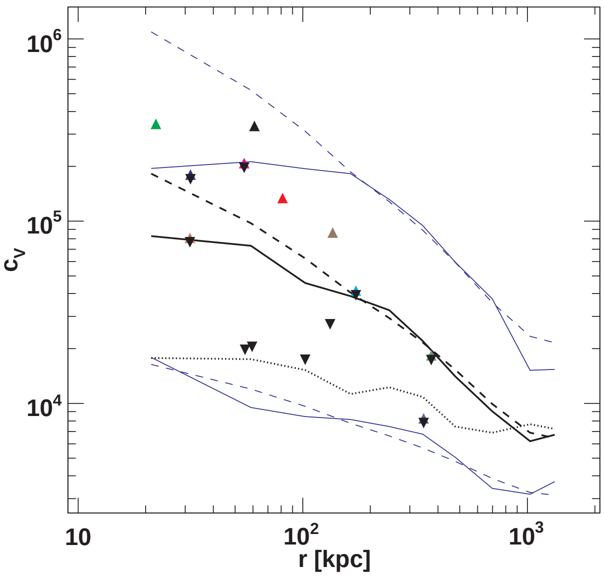

FIG. 9.— Median subhalo concentrations and 68% scatter (*solid lines*) versus distance from the Galactic center at the present epoch (average values over the last ten snapshots from $z = 0.05$ to $z = 0$). The dotted line shows 400 times the cosmic background density at the median formation times of these halos (see Figure 16). Finite numerical resolution limits concentrations to below a few times $10^5 \rho_{\rm crit}$ especially in the smaller satellites (the constant upper percentiles within 100 kpc are artificial). Dashed lines are fits (eq. 18) to the percentiles measured beyond 100 kpc. Likely dwarf galaxy host halos (triangles, same as in Figure 13) also follow the general relation.

halo regions, thereby reducing $r_{\rm Vmax}$ and increasing the mean density within this radius, c_V (Kazantzidis et al. 2004, see also Section 4). Together with the median, the 68% scatter in subhalo concentration is also growing. This may be caused by the increasing amount of mixing between newly infalling, low-concentration halos and strongly stripped, high-concentration clumps.

At $z = 0$ we find a clear trend for higher concentrations closer to the halo center, as shown in Figure 9. We use the following simple empirical fit to approximate this relation:

$$c_V(r) = a \left[\frac{\rho_{bg}(r)}{\rho_{\rm crit,0}}\right]^b , \qquad (18)$$

where ρ_{bg} is the average density of the corresponding spherical shell around the main host. The best-fit coefficients are $(a, b) = (5895, 0.33)$ for the median concentrations, (2997, 0.16) for the lower (16th) percentile, and (19370, 0.39) for the upper (84th) percentile.

The higher formation redshift of the inner halos is not enough to fully explain this concentration-radius relation. If we simply assume that the median halo concentrations are proportional to the mean cosmic density at the median formation epoch of these halos (dotted line in Figure 9) we do indeed get a qualitatively correct trend with radius, but the effect is not strong enough. Tidal interactions must significantly contribute to the final concentration versus radius relation. In § 4.3 we confirm that this is indeed the case: many halos did pass through the inner regions of the host at some earlier time and lost significant mass from tidal stripping. Interestingly, tides seem to increase the median concentrations (and scatter) even beyond $r_{200} = 389$ kpc (shells number 7 and 8). To summarize, the concentration-radius relation is caused by the combined effect of two different processes:

i) The formation of new small-scale structure stops when a shell collapses. Inner shells turn around and collapse earlier, and therefore contain earlier forming subhalos with a higher median concentration.

ii) Tidal interactions within the host halo increase subhalo concentrations.

4. EVOLUTIONARY TRACKS OF SUBHALOS

The parallel group finder 6DFOF (Diemand et al. 2006, 2007) finds peaks in phase-space density, i.e. it links the most bound particles inside the cores of halos and subhalos together. The same objects identified by 6DFOF at different times therefore always have quite a large fraction of particles in common. In most cases this fraction is over 90% between two subsequent Via Lactea snapshots (separated by 68.5 million years). This makes finding progenitors or descendants rather easy. When tracing halos backwards in time, we link a halo "A" to its main progenitor "B" only if A contains at least 50% of the particles in B and if B contains at least 50% of the particles in A. This definition is time symmetric and we use the same links when we follow halo histories forward in time. When a (sub)halo merges with a larger group its forward history ends with a special merger flag that points to the ongoing track of the merger remnant. We include in our analysis only halos larger than $V_{\rm max} = 5$ km/s at some point during their history. These halos are resolved sufficiently well so that one can follow both their smaller, high-redshift progenitors and also their present-day remnants, even if they did suffer large tidal mass loss. The well resolved sample selected this way contains 3883 halos, i.e. it is large enough to offer good statistics. Starting at $z = 0$ we identify the main progenitors of all such halos in each snapshot back to at least $z = 10$, when some progenitors start to become to small to be resolved and identified with 6DFOF. The dotted lines in the right hand panels of Figures 14 and 15 show the fraction of our halo sample for which we found a main progenitor as a function of time.

4.1. *Density profiles during tidal mass loss*

The evolution of the mass distribution in satellite halos undergoing tidal stripping is often studied within an external fixed potential (e.g. Dekel et al. 2003; Hayashi et al. 2003; Kazantzidis et al. 2004; Read et al. 2006). The resolution tests in Kazantzidis et al. (2004) show that numerical effects lead to significant additional mass loss when an infalling subhalo is resolved with N=0.5×10^6 particles and stripped down to a few thousand particles within a strong tidal field. The biggest subhalos in Via Lactea are almost as well resolved as the high resolution case in Kazantzidis et al. (2004). Many of the smaller ones lie far below their low resolution example and will suffer from artificial mass loss, especially when the tidal forces are strong, i.e. in the inner halo. Here we concentrate on the response to the tidal forces at pericenter passage of two of the largest, best resolved subhalos.

The first example is given is Figure 10. This subhalo was accreted near $a = 0.6$ and completes three pericenter passages before $z = 0$. Its full track is shown in Figure 12, while Figure 10 depicts the mass distribution around this subhalo as it completes its second pericenter passage at $a = 0.844$ ($r_{\rm peri} = 7.0$ kpc). The plot shows the mass enclosed within spherical windows of fixed physical radii as a function of time. Not all of the enclosed mass will be bound to the subhalo. At the peak of the 10 kpc line, for example, the majority of enclosed mass is associated to the underlying host, the density of which is is $5.5 \times 10^4 \rho_{\rm crit} = 8.3 \times 10^6\,{\rm M}_\odot/{\rm kpc}^3$ at 7.0 kpc. On the other hand the host contribution to the mass enclosed within 1 kpc is negligible compared to the subhalo's own contribution. The brief increase in enclosed mass for spheres with $r \simeq 1$ kpc shortly after pericenter passage reflects a temporary contraction of the subhalo as a response to the rapidly varying potential, the so called tidal shock (e.g. Gnedin & Ostriker 1997). This contraction is only temporary, and shortly afterwards the mass in the affected spheres actually decreases. The energy input from the tidal shock results in a net expansion (e.g. Hayashi et al. 2003; Faltenbacher et al. 2006)[9].

Particles in the outer regions of the satellite complete only a tiny fraction of their orbit around the subhalo center during the duration of the tidal shock. For these particles the tidal shock is impulsive and results in a maximal energy change. Particles near the subhalo center are less affected, since their internal orbital period is shorter than the duration of the shock. According to Gnedin & Ostriker 1997, the energy input is proportional to

$$\Delta E(r) \propto [1 + \omega(r)\tau]^{-5/2} \ , \qquad (19)$$

where $\tau = \pi r_{\rm peri}/V_{\rm peri}$ is the duration of the tidal shock and $\omega = v_{\rm circ}(r)/2\pi r$ is the inverse of the circular orbit time in the subhalo. For the small pericenter in this example the shock duration is only $\tau = \pi$ (7.0 kpc)/(500 km/s) = 42.9 Myr. This matches the subhalo orbital time at $r_{\rm eq} = 0.20$ kpc, i.e. at this scale $\omega(r)\tau$ equals one and $\Delta E(r)$ is reduced to 0.18 of the maximal value. Particles inside of $r_{\rm eq} = 0.20$ kpc should be less affected by the shock, unfortunately we cannot probe such small scales reliably. We do see however, that the shock is stronger in the outer halo: the mass within 1 kpc drops to a new constant value of 0.79 times the mass before the pericenter passage. Farther out the mass loss is larger: at $a = 0.9$ the mass within 10 kpc is only 52% of the value before the pericenter. Therefore the remnants of such a strong tidal interaction end up having lower densities at most radii, but with steeper, more concentrated density profiles since more mass is removed from the outer regions.

Before this pericenter passage the satellite has $r_{\rm Vmax} =$ 7.5 kpc. Its tidal radius at pericenter is much smaller, only 1.6 kpc. According to Hayashi et al. (2003), satellites are fully disrupted when $r_t < 2r_s \simeq r_{\rm Vmax}$ at pericenter. This is clearly not the case in our example: the satellite survives this pericenter passage [10], even though the tidal radius at pericenter is 4.7 times smaller than $r_{\rm Vmax}$. Figure 12 shows that in general satellites survive even if they have several close pericenter passages like the one studied here. In § 4.6 we find that total subhalo disruption happens very rarely, if at all.

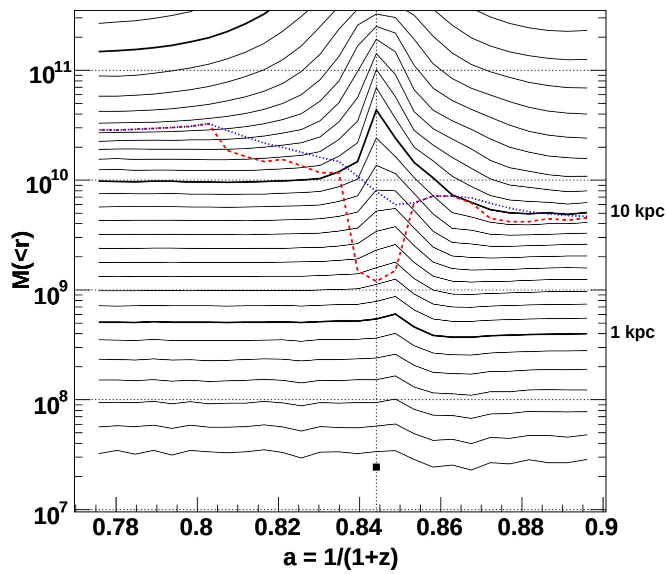

Fig. 10.— Evolution of the mass distribution (*solid lines*) and tidal mass (*dashed line*) of a subhalo undergoing strong tidal forces. The thick solid lines show the mass enclosed within 1.0 and 10 kpc spheres around the subhalo center. The thin solid lines correspond to the mass within nine intermediate radii (1.3,1.6, 2.0, 2.5, 3.2, 4.0, 5.0, 6.3 and 7.9). The smallest radius shown is 0.251 kpc, which is 2.8 times the force resolution. This halo approaches the Galactic center to within 8.3 kpc at $a = 0.844$ (*vertical dotted line*). Tidal mass loss is larger in the outer parts, but also the inner subhalo loses mass. In response to the strong tidal shock the satellite contracts just after the pericenter and expands soon after. The mass retained at $a = 0.9$ is 3.9 times larger than the mass within the tidal radius at the pericenter. A "delayed" tidal mass (*dotted line*) may be a better approximation to the bound mass. At $r_{\rm eq} = 0.20$ kpc (*square*) the subhalos internal orbital timescale matches the duration of the tidal shock. (see main text for details).

The second example is given is Figure 11. This subhalo fell into the main host at $a = 0.7$ and completes only one relatively distant pericenter passage at $a = 0.830$ ($r_{\rm peri} = 58.3$ kpc). Its track is shown in Figure 12. The tidal forces at these distances are much weaker, and as a result there is no significant mass loss in the inner parts (less than 10% within 1 kpc) and only mild mass loss in the outer parts (29% within 10 kpc). A tidal shock can still be identified, but it is less strong and because of the longer shock duration it does not reach as far in as in the previous example. In this case $\tau = \pi(56\,{\rm kpc})/(423\,{\rm km/s}) = 406$ Myr and $r_{\rm eq} = 2.0$ kpc. The increase at 10 kpc is purely due to the background density that peaks at $2.1 \times 10^5\,{\rm M}_\odot/{\rm kpc}^3$ at pericenter. The shells around 3 kpc do show some contraction and expansion caused by the weak shock. Radii smaller than $r_{\rm eq} = 2.0$ kpc are practically unaffected by the shock. The mass retained at $z = 0$ is larger (by a factor of 1.8) than the mass within the tidal radius at pericenter: 10% of this mass is contributed by the host local background density at the position of the subhalo, and the remaining 90% can be attributed to the subhalo itself. Remarkably, we find that the fraction of particles gravitationally bound to the subhalo (determined with

[9] The expansion is large enough to overcome any tidal compression suggested for subhalos orbiting in a $\Phi \propto r$ potential, as in the $\rho \propto r^{-1}$ inner region of the host halo (Dekel et al. 2003).

[10] It even survives the subsequent, closer pericenter at only 5.2 kpc.

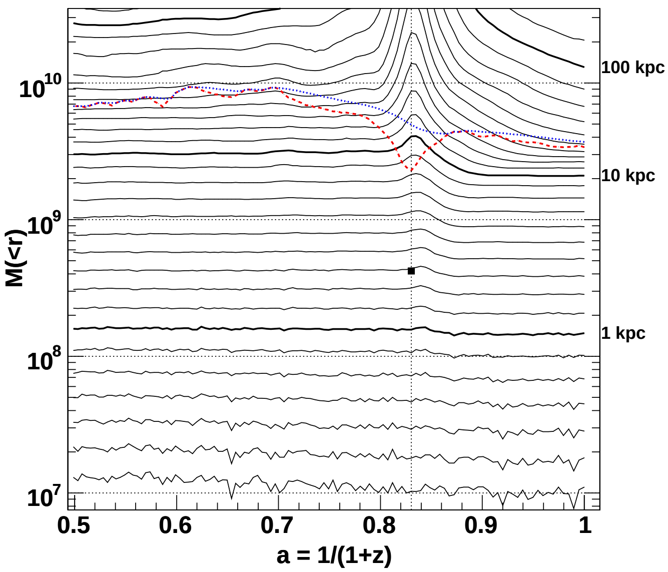

FIG. 11.— Evolution of the mass distribution (*solid lines*) and tidal mass (*dashed line*) of a satellite undergoing weak tidal forces. This object falls into the host and has only one pericenter passage at 56 kpc and $a = 0.83$ ($z = 0.20$). The track of this subhalo is given in Figures 12 and 13 (dark green in the color version). Tidal mass loss is large in the outer halo, while the inner subhalo remains unaffected.

SKID[11]), is also 90%. Looking for additional bound material beyond the $z = 0$ tidal radius increases the bound mass of the subhalo slighly: by 28% when going out to 2.5 times the tidal radius. This larger bound mass is 16% higher than our tidal mass estimate, which includes the 10% contribution from the host halo.

The tests discussed above suggest that the simple tidal mass estimates are a good approximation (within 20%) to the bound mass at most times. During pericenter passage our tidal mass may underestimate the bound mass by factors of about 2 to 4. The same problem would affect subhalo finders based on density only, since the bound material that is missed by the tidal criterion by definition lies near (within a factor of two) or below the host local background density. As a result subhalos at pericenter get assigned too little mass, and smaller subhalos might be missed altogether. Our 6DFOF, in contrast, always finds small groups, even when they lie below the background density. In the current implementation, however, we also do not assign enough mass to them.

The transient dip in tidal mass during pericenter passages seen in these two examples occurs because tidal stripping is not instantaneous; many particles remain bound, even though they lie beyond the tidal limit when the subhalo is near pericenter. Some semi-analytic subhalo models incorporate this effect by removing only a certain fraction of the extra tidal subhalo mass at each time step δt:

$$\Delta m_d = M(> r_t)\delta t / T_s \ . \tag{20}$$

T_s is the time-scale for tidal stripping. We calculate the extra tidal mass $M(> r_t)$ by subtracting mass that lies within the tidal radius in the current snapshot from the "delayed" tidal subhalo mass m_d at the previous snapshot. m_d would be identical to the tidal mass in the limit of very rapid tidal stripping ($T_s \rightarrow \delta t$). T_s is often assumed to be equal to the satellite orbital time (e.g. Taylor & Babul 2001; Zentner & Bullock 2003) [12]. Both of our (quite different) examples suggest that the stripping timescale is about six times shorter than the time it takes the satellite to complete one full orbit ($T_{\rm orbit}$). The delayed tidal masses assuming $T_s = T_{\rm orbit}/6$ are shown with dotted lines in Figures 10 and 11. This means that mass loss can be relatively quick, e.g. it is possible for a subhalo to lose more than half of its mass during only a tenth of the time it takes to complete one orbit.

4.2. *The hosts of Milky Way dwarf satellites*

A promising scenario to explain the low numbers of Local Group dwarf galaxies relative to the abundance of CDM subhalos (Moore et al. 1999; Klypin et al. 1999), is to suppress star formation in small halos below a filtering mass that increases after reionisation (Kravtsov et al. 2004). Similar models (Bullock et al. 2000; Moore et al. 2006) select only systems above the atomic cooling mass at the reionisation epoch ($z \simeq 10$). This too yields a realistic $z = 0$ dwarf galaxy population and the disrupted building blocks are shown to match the spatial distribution and kinematics of halo stars around the Milky Way (Diemand et al. 2005; Moore et al. 2006). In the Kravtsov et al. model the ten most luminous dwarfs are practically all found in the subhalos that had the largest peak circular velocities before these subhalos were affected by tides. The mild time-dependence of the filtering mass only leads to a few exceptions from this simple rule.

To illustrate the evolution of the hosts of dwarf galaxies in such scenarios we select two samples consisting of ten objects. The "largest before accretion" (LBA) sample is made up of the ten systems with the highest $V_{\rm max}$ throughout the entire simulation. These ten systems all reached $V_{\rm max} > 37.3$ km/s at one time. The "early forming" (EF) sample consists of the ten halos with $V_{\rm max} > 16.2$ km/s (the atomic cooling limit) at $z = 9.6$. The EF sample corresponds to the Moore et al. (2006) model, where sudden reionisation is assumed to have a strong effect on dwarf halos. The LBA scenario corresponds to allowing star formation only above a relatively high, constant critical size, a scenario of permanently inefficient galaxy formation in all smaller systems, independently of time-dependent changes in the environment like reionisation. The Kravtsov et al. (2004) model would yield a selection that is intermediate between the LBA and EF samples.

Six out of ten objects turn out to be the same in both samples. Because of the evolution of $V_{\rm max}(z)$ during the growth of halos at high redshift, it is often the case that the ones reaching the largest sizes before accretion are also the ones that have the largest $V_{\rm max}(z \simeq 10)$. To avoid redundancy we plot the time evolution only for the EF sample, but show the $z = 0$ properties of the LBA sample for comparison (Figures 12 and 13). The subhalo histories are obviously very diverse. These halos have completed between zero and ten pericenter pas-

[11] Available at http://www-hpcc.astro.washington.edu/tools/skid.html.

[12] The time-scale used in Zentner et al. (2005) is shorter: $T_{\rm orbit}/3.5$. A factor of 2π is missing in their Eq. 8 (A. Zentner, private communication)

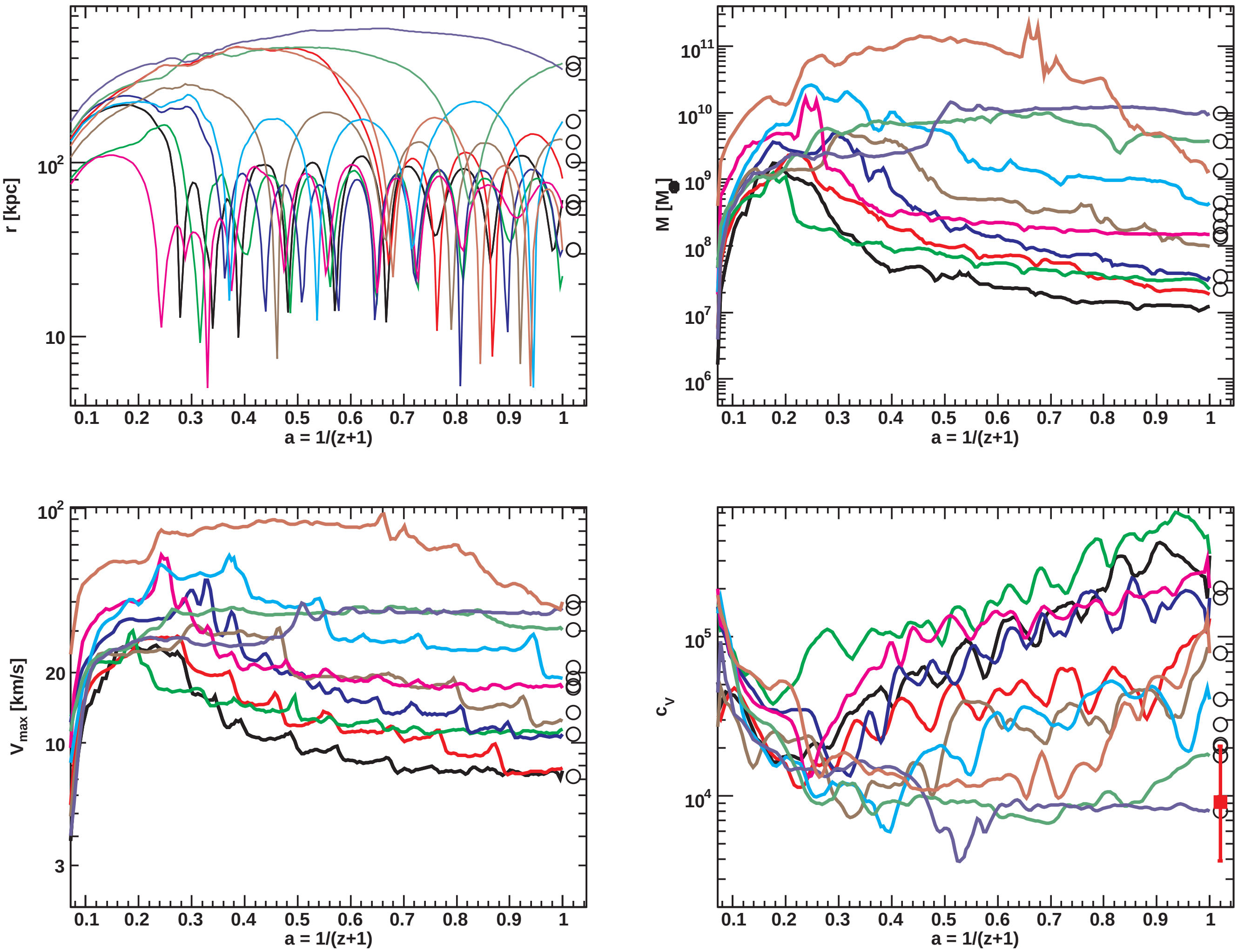

FIG. 12.— Evolutionary tracks of the earliest forming substructure (EF sample, *lines*) and $z = 0$ properties of the subhalos with the largest peak circular velocities before accretion (LBA sample, *circles*). *Top left panel*: distances to Galactic center versus cosmic expansion factor. Pericenter distances were calculated from the nearest snapshot (see §4.5). *Top right*: evolution of tidal masses (or M_{200} for halos in low density environments, i.e. whenever M_{200} is smaller than the tidal mass). *Bottom left*: evolution of subhalo peak circular velocities. *Bottom right*: evolution of subhalo concentrations. Square with error bars gives the median and 68 % scatter of concentrations measured in field halos at $z = 0$.

sages. Some have lost over 99% of their mass, others no mass at all. The peak velocity $V_{\rm max}$ may have been reduced by up to a factor of six, or not at all. Mass loss is often largest at the first pericenter passage (or the first few) and then becomes smaller except for the largest subhalo, the orbit of which is decaying quickly because of dynamical friction (e.g. Taffoni et al. 2003). All halos except one undergo pericenter passages that can lead to tidally induced changes in galaxy morphologies (Mayer et al. 2001a,b). For dwarf host halos found near the Galactic center today tidal interactions were more violent, happened more often and started earlier, consistent with the very large mass-to-light ratios found for some inner dwarf satellites (Mayer et al. 2007).

Concentrations decline with time while halos are growing. Later they remain constant for systems that lose no or only little mass and end up in the range where field halo concentrations are found (measured at $z = 0$ between 1.5 and 4 times r_{200} using all systems with $V_{\rm max}$ between 6.6 and 15 km/s). For systems with large mass loss, on the other hand, the concentrations increase with time and end up significantly above the field halo range. Figure 13 illustrates the increase in concentration during tidal stripping in the $V_{\rm max} - r_{\rm Vmax}$ plane. With our definition of concentration c_V (eq. 7), this parameter remains constant along $V_{\rm max} \propto r_{\rm Vmax}$ tracks. In the $V_{\rm max} - r_{\rm Vmax}$ plane, halos start in the lower left corner at high redshift and then wander quickly towards the upper right corner. During this active mass-growth phase $r_{\rm Vmax}$ increases by a larger factor than $V_{\rm max}$, i.e. the concentration c_V decreases. After their active mass-growth phase they remain stationary in the upper right corner of this plane, until they experience tidal mass loss. Perhaps surprisingly, those satellites that do undergo tidal stripping retrace their paths in the $V_{\rm max} - r_{\rm Vmax}$ plane. This means that tidal stripping seems to exactly undo the inside out subhalo assembly by removing mass from the outside in. Each stripped down $z = 0$ remnant ends up resembling its own high redshift progenitor. Furthermore these $z = 0$ remnants have high concentrations, typical

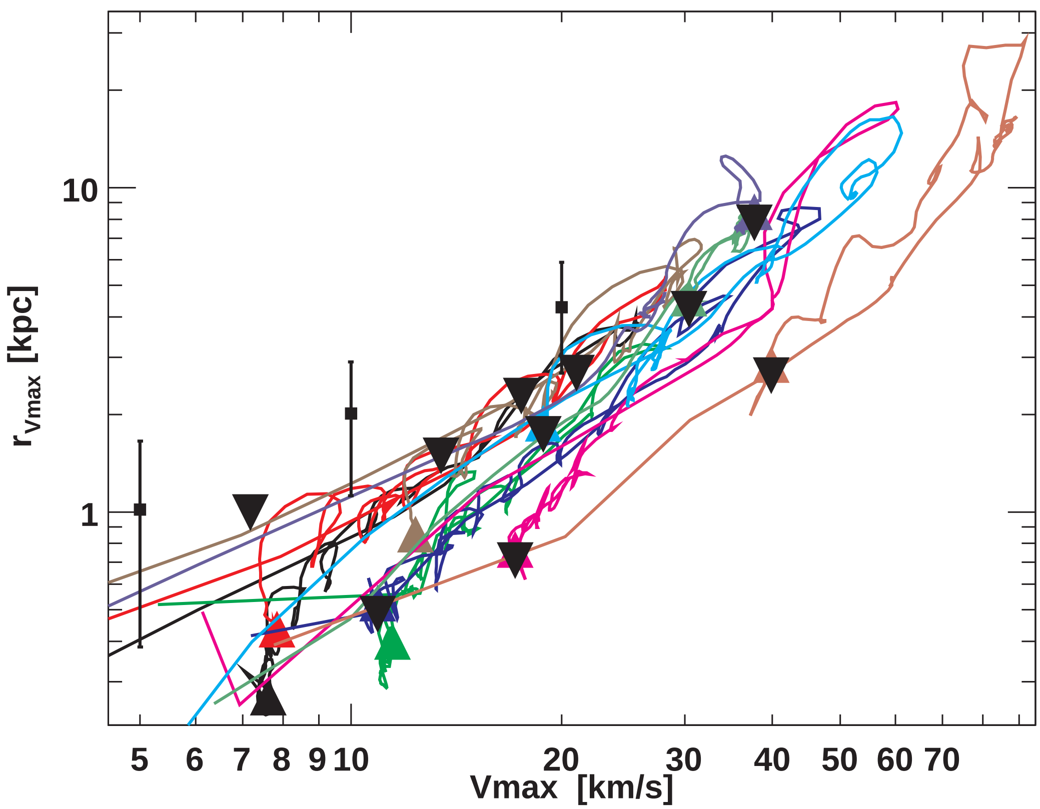

FIG. 13.— Evolution in the $V_{\max} - r_{V\max}$ plane of likely dwarf galaxy host halos (the EF sample, see text for details). Tracks start at high redshift when halos are still small, i.e. in the lower left corner of this plot. End points of the tracks at $z = 0$ are marked with upward triangles. Only the end points are shown for the LBA sample (*downward triangles*). Each halo tends to grow and shrink within the same region of this plane, i.e. the end points resemble their (relatively concentrated) high redshift progenitors. Squares with error bars show the median location of $z = 0$ field halos and the 68% scatter. Tidal stripping produces halos that are more concentrated than those in the field (i.e. smaller $r_{V\max}$ at a given $V_{\max}$).

of high redshift systems, and clearly higher than present-day halos that did not suffer significant mass loss. Both samples follow the concentration-radius relation (see Figure 9), i.e. the highest concentrations are found in subhalos near the Galactic center.

The differences between the two samples are small and presumably hard to detect from Local Group observations: at $z = 0$ the four EF halos that are not part of the LBA sample have smaller masses and lower $V_{\max}$ but larger concentrations than the four LBA satellites that aren't part of the EF sample. Unfortunately, current Local Group dwarf galaxy mass models (e.g. Łokas et al. 2005; Kleyna et al. 2005; Koch et al. 2007) , based on radial velocity and surface brightness data, can only place weak constraints on $r_{V\max}$ (Strigari et al. 2006; Penarrubia et al. 2007). In both samples the hosts of the most luminous dwarf galaxies are significantly more concentrated than field halos of similar mass: all ten c_V's lie above the field halo median, and most (nine for EF, seven for LBA) lie above the mean halo scatter. Taking the higher concentrations of subhalos into account is important when estimating the $V_{\max}$ values of dwarf galaxy halos (Strigari et al. 2006); using field halo concentrations instead (Penarrubia et al. 2007) leads to higher $V_{\max}$ values.

4.3. *Ensemble-averaged evolutionary tracks*

After the few individual examples discussed above we now go on to present ensemble-averaged evolutionary tracks, determined from a large number of subhalos. The tracks are selected by two criteria: the (sub)halo $V_{\max}$ must be at least 5 km/s at some time, and the object must end up in one of the ten spherical shells around the main halo.

Figure 14 show the median track of halos ending up within the first six shells, i.e. within $r_{200} = 389$ kpc. Median radii and 68% scatter illustrate where most subhalos lying in a given shell today were located in the past. Subhalos in the two innermost shells at $z = 0$ spend most of their time outside of these shells, i.e. most of these satellites are on more extended orbits and are near their pericenter at $z = 0$. The median radii in shells 3 to 6 are roughly constant since $a = 0.5$, i.e. the orbits of subhalos that lie within one of these shells today were distributed roughly symmetrically around this radial shell at earlier times. The scatter indicates that the typical peri- and apocenters lie outside the final shell, which is not surprising given the nearly isotropic orbits and the median ratio of apocentric to pericentric radii of 1:6 (see §4.5).

The radii also reveal some regularities between current positions and infall time. Halos in shell 1 today for example, are quite unlikely to have fallen in around $a = 0.6$ (and obviously also after $a = 0.9$). Those who did fall in around $a = 0.6$ are most likely found in shells 3 to 6

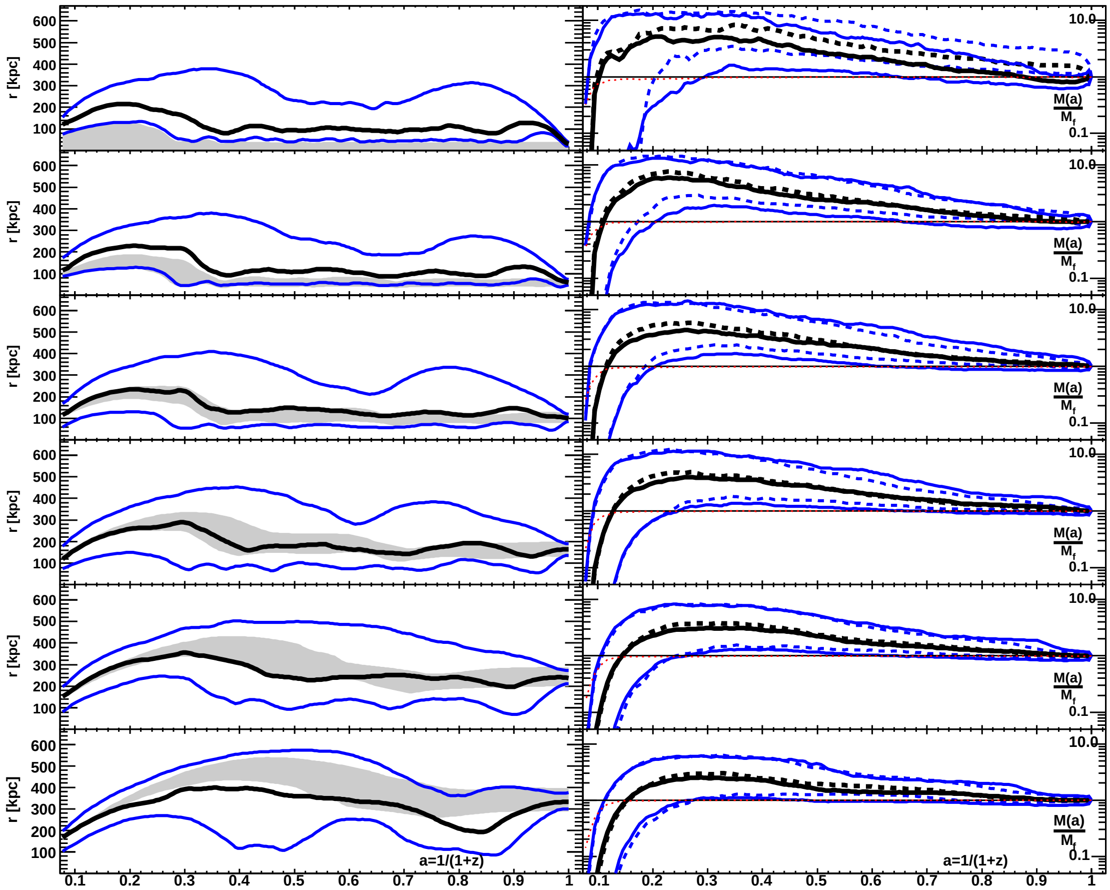

Fig. 14.— Evolution of (sub)halos that end up in the same radial shell at $z = 0$. Shells 1 to 6 are shown from top to bottom. Left panels show median and 68% scatter of (sub)halo distances from the center of the host halo. Due to their radial orbits, subhalos are often found outside of the fixed mass shell (*shaded region*) in which they end up at z=0. Right panels show median and 68% scatter of the fraction of current mass to final mass (*dashed lines*) and the one-fourth power of the fractions of peak circular velocity (*solid lines*). The *thin dotted lines* show the fraction of halos we are still able to trace at a given epoch. Halos without resolved main progenitor are not included in the median radii, but they are counted as zero when the medians of mass and peak circular velocity fractions are calculated.

at $z = 0$, after having completed one pericenter passage (for an example, see the track near 400 kpc at $a = 0.6$ in Figure 12).

In order to show how subhalo masses evolve, we follow two mass indicators over time. One is simply $M(a)/M(a = 1)$, the ratio of the subhalo's mass at a given time to its mass today. The other is based on the ratio of peak circular velocities, $[V_{\rm max}(a)/V_{\rm max}(a = 1)]^4$. The later definition is motivated by the result that during tidal mass loss the peak circular velocity decreases roughly like $V_{\rm max} \propto M^{1/4}$ (Hayashi et al. 2003; Kazantzidis et al. 2004; Kravtsov et al. 2004). Whenever this approximate scaling holds for our two mass indicators, they evolve proportional to each other.

We have plotted the median and 68% scatter of these two mass indicators versus scale factor in the right hand panel of Figure 14. In the outer regions near r_{200} the two do indeed agree nicely, but closer to the halo center the masses are more strongly reduced than the peak circular velocities. At least in the innermost bin the tidal masses seem to underestimate the bound masses. From the median radii (left panel) it is clear that most of the halos in this shell are at pericenter today, while in section 4.1 we show that our definition of tidal mass tends to underestimate the true bound subhalos mass at pericenter. This explains the quick dip in the median mass fraction by almost a factor of 2 near $z = 0$.

Not surprisingly, both the median mass and $V_{\rm max}$ fractions show clearly that tidal stripping is stronger near the halo center. Stripping was also stronger at high redshifts: the median $V_{\rm max}$ are roughly constant after $a = 0.7$. In shells 3 to 6 both the median $V_{\rm max}$ and median radii are roughly constant after $a = 0.6$. This supports the findings of Section 3, that subhalo and host halo evolution are closely linked. Early on the host system undergoes an active phase of merging and mass accretion, during which the subhalos are accreted and their mass is reduced quickly by tidal stripping at the first pericenter passage (Section 4.5). Once the host halo has formed there is little physical mass redistribution or accretion and the subhalo population becomes stationary. During this quiet epoch most subhalos move on stable orbits and their mass loss is relatively small.

4.4. *Formation histories and environment*

Figure 15 shows the ensemble-averaged orbital history of halos beyond r_{200} today (in radial shells 7-10). According to their current location these would be considered "field" halos. However, many of them have actually orbited through the host halo at some earlier time. The resulting tidal interactions halted their growth and in many cases even reduced their mass and $V_{\rm max}$. Such "former subhalos" would be classified as very early forming

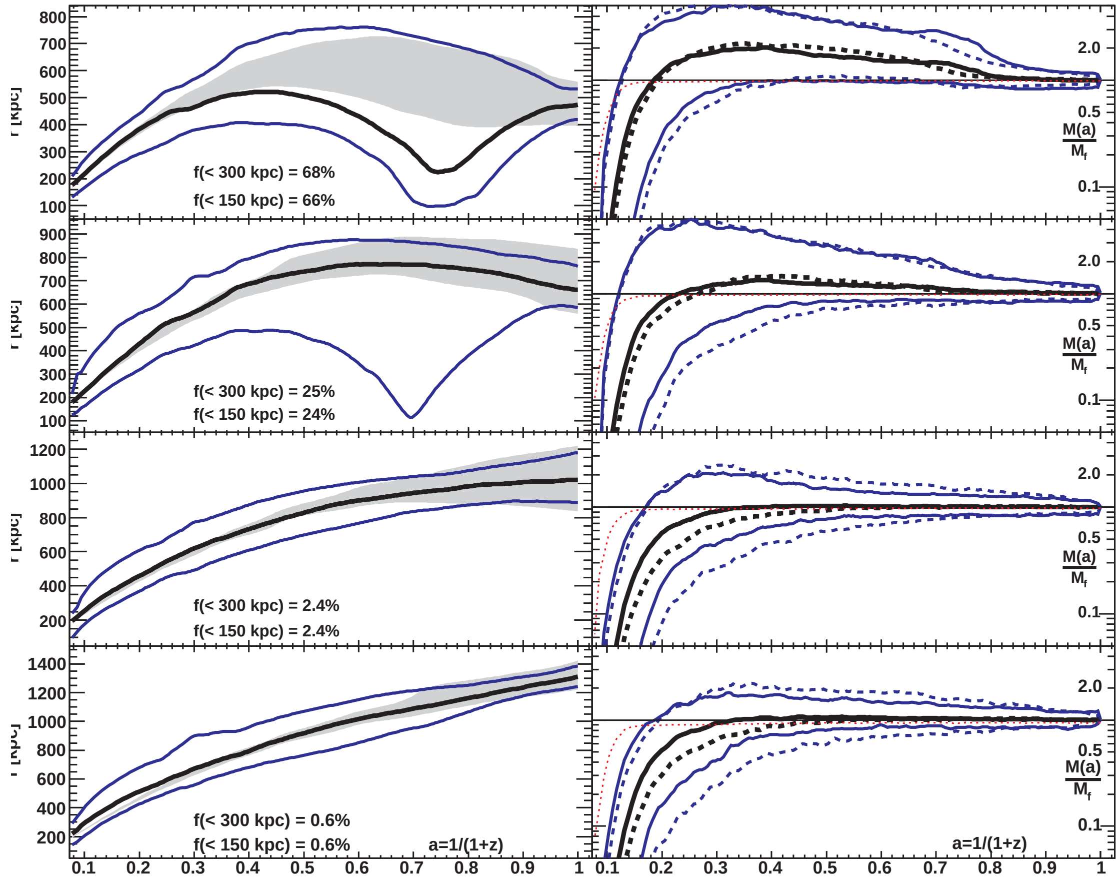

FIG. 15.— Same as Figure 14, but for shells 7 to 10 that lie beyond $r_{200} = 398$ kpc at $z = 0$. However, many of the "field" halos in shells 7 and 8 were actually "subhalos" at some earlier time. The left panels contain include the fractions of halos that approached the galaxy halo to within 300 and 150 kpc anytime after $z = 1$. Such former subhalos have a reduced mass (and $V_{\rm max}$), due to tidal interactions with the main host at some earlier time. According to common definitions of halo formation time these stripped former subhalos would be classified as very early forming "field" halos.

field halos according to common definitions of formation time, because they reached a given fraction of their current, tidally reduced, mass or $V_{\rm max}$ much earlier than the average "real" field halo that never passed through the host system. The population of "former subhalos" is significant: around galaxy clusters half of all halos found between one and two virial radii today have passed through the cluster at least once (Balogh et al. 2000; Moore et al. 2004; Gill et al. 2005), and for Via Lactea's subhalos this fraction is even larger, 0.74. The fraction is very similar when only the most massive (sub)halo orbits are used, i.e. we found no (sub)halo mass dependence.

This illustrates clearly that a halo affects the formation histories of many systems that are not within its virial radius (anymore). In other words, the assembly history of CDM halos must depend on their environment. Such correlations have indeed been quantified recently in terms of stronger clustering of early forming sub-M_* halos (Gao et al. 2005) and as earlier median formation times in high density environments (Sheth & Tormen 2004; Harker et al. 2006). Both studies are based on formation times defined relative to the $z = 0$ halo properties, analogous to our z_{85} definition (eq. 5). This definition of formation time correlates strongly with mean environment density in and around the Via Lactea halo, as seen in Figure 16, where we plot median formation times in our ten radial shells (cf. Figures 14 and 15) as a function of the mean density in these shells.

On the other hand, for a formation time based on prestripping halo properties, $z_{\rm form}$ (eq. 4), this correlation disappears for halos outside today's virial radius. It is maintained inside the host halo because halos form before they are accreted and median accretion redshifts are higher for subhalos that end up in the inner shells (see Figure 14). Note that the median $z_{\rm form}$ lies below z_{85} even in shells 9 and 10 where only very few halo (2.4 % and 0.006 %, respectively) interacted with the primary halo. This may be due to tidal interaction with a few other relatively large ($V_{\rm max} \simeq 70$ km/s) halos in the outskirts of Via Lactea.

To summarize, we confirm the (Balogh et al. 2000; Moore et al. 2004; Gill et al. 2005) result that many subhalos end up in the field (according to common definitions) and we illustrate that this leads to a clear environment dependence of halo assembly histories like those found in (Gao et al. 2005; Harker et al. 2006). A related explanation for the age dependence of halo clustering based on tidal interactions with larger halos was recently proposed by Wang et al. (2006). Defining halo formation times relative to the maximal size a halo had over its lifetime removes the environment dependence of median formation times. Nevertheless, this does not change the Gao et al. (2005) conclusion, that knowing only the $z = 0$ mass of a halo is not sufficient to infer its accretion

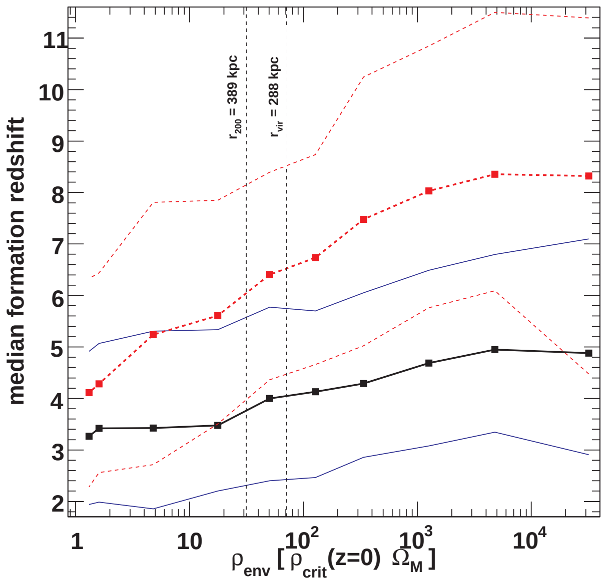

FIG. 16.— Median $z_{\rm form}$ (*solid lines*) and z_{85} (*dashed lines*), both with 68% scatter versus environment density. Using z_{85}, defined so that $V_{\rm max}(z_{85}) \equiv 0.85 V_{\rm max}(z=0)$, suggest that halos and subhalo living in denser environments today (i.e. closer to the Galactic center) have formed earlier. The relation holds at all environments probed here, even well beyond the virial radius of the main halo. Using the pre-stripping halo size to define the formation time $z_{\rm form}$ the relation is only significant within the virial radius.

history or halo occupation distribution in a statistically correct way. Due to the strongly nonlinear tidal origin of this effect it seems difficult to correct the analytical approximations, suggesting that simulations should be employed whenever structure formation needs to be followed accurately.

4.5. *Mass loss per pericenter passage*

In this Section we quantify how much mass a subhalo loses per pericenter passage. We use the same sample of 3883 relatively well resolved ($V_{\rm max} > 5$ km/s at some redshift) subhalos as before. Pericenters are defined as local minima in the distance to the main progenitor. Only minima within $4r_{V\rm max}(z)$ are counted, to exclude minima caused by orbits around other progenitors. The time between stored snapshots (68.5 Myr) is too large to capture all of the smaller pericenters. We calculate them by integrating orbits using the position and velocity of the subhalo and the spherically averaged mass distribution of the host halo at the nearest snapshot. The 68% interval of the directly measured $r_{\rm apo}/r_{\rm peri}$ distribution is nearly identical (within 0.01) as the corrected one, i.e. for most subhalos the calculated pericenter is similar to the one at the nearest snapshot. Our subhalos made up to 14 such pericenter passages, but most of them have completed only a few pericenters, or none at all (see Figure 17). The ratios of pericenter and subsequent apocenter radii show that most subhalo orbits are quite radial. The median ratio of our direct measurement (0.169) agrees very well with the derived value 1:6 from Ghigna et al. (1998), who used $z = 0$ subhalo positions and velocities and the spherically averaged host density profile to integrate subhalo orbits approximately. The 90% interval extends from 0.035 to 0.666, i.e. only 5% of all subhalo orbits are

	all pericenters	1. pericenter	last of several
$\delta V_{\rm max}$	0.14±0.11	0.22±0.11	0.10±0.08
δM	0.41±0.22	0.58±0.20	0.31±0.18
$\frac{r_{\rm peri}}{r_{\rm apo}}$	$0.169\,^{0.395}_{0.070}$	$0.133\,^{0.305}_{0.053}$	$0.159\,^{0.336}_{0.078}$
$\frac{r_{\rm peri}}{r_{V\rm max}}$	$0.25\,^{0.35}_{0.13}$	$0.24\,^{0.35}_{0.12}$	$0.27\,^{0.36}_{0.15}$
$z_{\rm peri}$	$0.67\,^{1.54}_{0.28}$	$1.23\,^{2.20}_{0.61}$	$0.27\,^{0.42}_{0.15}$

NOTE. — Mean and rms scatter are given for the decrease in $V_{\rm max}$ per orbit $\delta V_{\rm max}$ and the mass loss δM. For the other quantities the median and the 68% interval are listed.

rounder than about 2:3. These ratios are similar when we include only the last of several orbits (Table 4.5). When we include only the first pericenter passages the ratios are slightly smaller, the median is 0.133. The anisotropy parameter $\beta(r)$ is about $\beta(r) \simeq 0.55(r/r_{\rm vir})^{1/3}$ for these subhalos (and also for the total the dark matter) from $r/r_{\rm vir} \simeq 0.2$ to 1.0. The positive β values indicate radially anisotropic subhalo (and dark matter) velocity distributions, and the anisotropy increases with radius.

Masses (and $V_{\rm max}$) are measured at the apocenter after the pericenter passage (t_f), and at an earlier time (t_i), so that the pericenter lies in the middle of these two times. This way we compare masses measured within similar, low background densities (even when a subhalo falls in for the first time) and we avoid the problem of underestimating the subhalo mass at pericenter (see §4.1). We do not use late pericenter passages, i.e. when no subsequent apocenter is reached before $z = 0$. Mass loss is expressed as $\delta M \equiv [M(t_i) - M(t_f)]/M(t_i)$ and the reduction in subhalo peak circular velocity $\delta V_{\rm max}$ is defined accordingly. Figure 17 shows that the average mass loss (and the decrease in $V_{\rm max}$) per pericenter is larger for orbits with smaller pericenter distances. The scatter is quite large, the rms scatter is about 0.22 in each radial bin (0.11 for $\delta V_{\rm max}$). The average mass loss also depends strongly on the history of a subhalo: it is significantly larger when a subhalo passes through pericenter for the first time (Figure 17 and Table 4.5). The mass loss during the last of several orbits, on the other hand, lies significantly below the average over all orbits. Many of the individual tracks in Figure 12 illustrate this behavior, i.e. they show a large early mass loss and nearly constant masses (and $V_{\rm max}$) near $z = 0$. The effect also manifests itself in the larger average mass loss before $a = 0.6$ in Figure 14, it is however smeared out because the first pericenters occur over a wide range of redshifts (the 68% interval extends from $a = 0.31$ to $a = 0.63$), which is earlier but overlapping largely with the distribution of all other pericenters (68% within $a = 0.48$ to $a = 0.81$).

4.6. *Tracing survival and merging forward in time*

The individual and ensemble-averaged tracks studied earlier by definition only include halos that have survived (meaning they have a remnant above our resolution limit) until today. This could potentially bias the reported median mass loss rates to lower levels. In this Section we quantify how many halos were stripped below our resolution limit and check if this reduces the mass loss reported for the survivors in the previous section. We select halos with peak circular velocities above 10 km/s at $z = 1$ and look for their remnants today. Selecting only well resolved halos is necessary for two reasons:

i) tidal stripping and destruction are overestimated

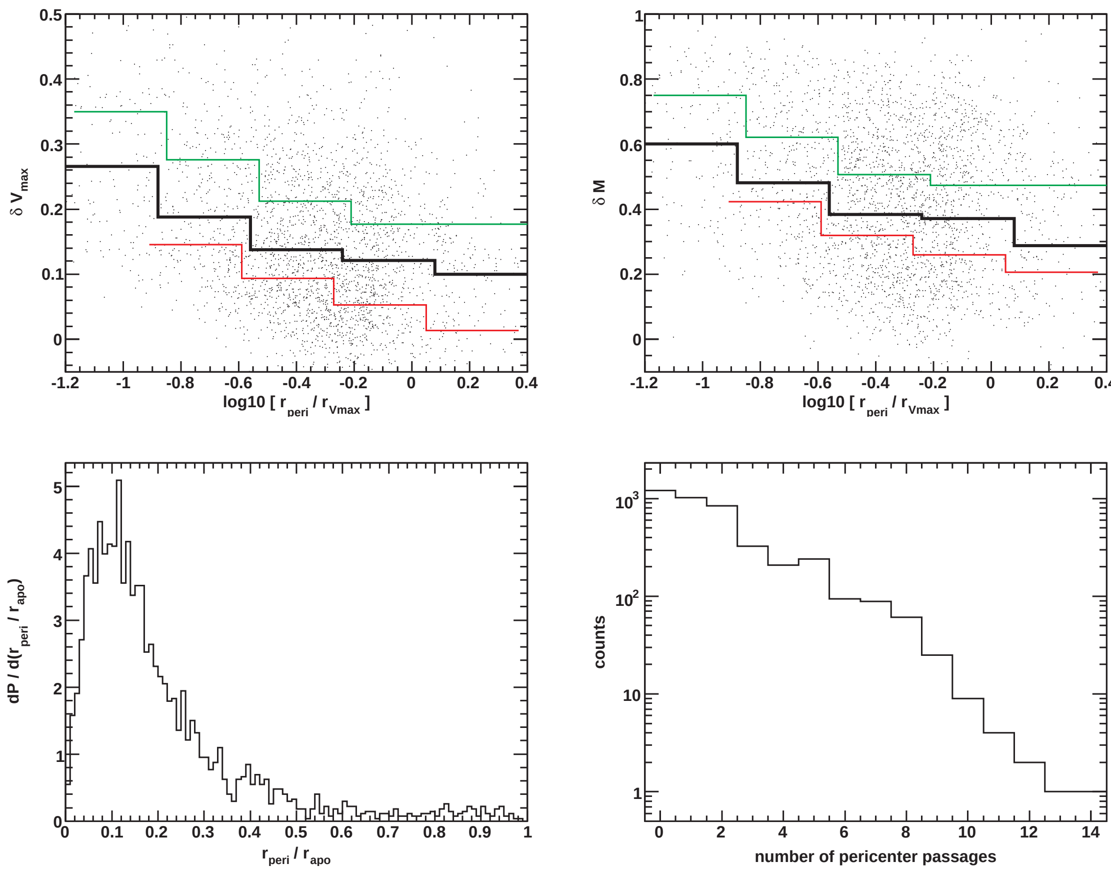

FIG. 17.— *Upper left panel*: decrease in $V_{\rm max}$ per orbit versus pericenter distance. *Upper right panel*: mass loss per orbit versus pericenter distance. In both upper panels we show averages over all orbits (*thick solid lines*), over first orbits (*upper thin lines*) and over the last orbit of those subhalos that complete more than one orbit (*lower thin lines*). Pericenter distances are normalized to $r_{\rm Vmax}(z_{\rm peri})$. Using a fixed scale like $r_{\rm Vmax}(z=0) = 69$ kpc gives very similar results since $r_{\rm Vmax}$ is roughly constant since the last major merger at $z \simeq 1.7$. The lower left panel gives the ratios of pericenter distance to distance at the subsequent apocenter and the lower right panel shows how many pericenter passages were completed by the 3883 subhalos in our sample.

due to numerical effects in barely resolved subhalos (the "overmerging problem" Moore et al. 1996; Kazantzidis et al. 2004).

ii) one needs to identify the remnants even after severe tidal mass loss.

At $z = 1$ there are 241 subhalos with $V_{\rm max} > 10$ km/s within a sphere containing the final host halo mass (i.e. within shells 1-6). 232 of these are main progenitors of surviving subhalos, and two merge into a larger surviving subhalo between $z = 1$ and $z = 0$. Only the remaining seven subhalos are stripped below our resolution limit and disappear from our $z = 0$ sample. Half of the debris from the tidally disrupted satellites are concentrated within a sphere of only 52 kpc around the Galactic center (for comparison, the half-mass radius of the halo is 124 kpc), and the material beyond 52 kpc lies in three tidal streams oriented towards the center. Both the concentration of the debris and the radial direction of the streams suggest that the destruction happened close to the Galactic center. Extending the sample size by including all 1542 subhalos with $V_{\rm max} > 5$ km/s at $z = 1$ yields similar results: 2.4 % are lost and 1.3 % merge into a larger subhalo.

Since about 97% of the subhalos selected at $z = 1$ survive, the average evolutionary tracks of surviving systems given in Section 4.3 are representative for the majority of subhalos. It is also interesting to note that subhalo mergers are extremely rare, between $z = 1$ and $z = 0$ the merger fraction is only about 1.3 %.

Using the same subhalo selection we can also study what fraction of their $z = 1$ mass remains bound to their $z = 0$ remnants. It turns out that this fraction depends strongly on the initial mass range of the selected subhalos. Larger subhalos retain less of their mass (Figure 18). The most massive halo (light brown track in Figure 12) has an orbit that decays quickly due to dynamical friction and it loses most of is mass (98.9%) between $z = 1$ and $z = 0$. Smaller subhalos are less affected by dynamical friction and lose significantly less mass. The increase in mass loss for subhalos with $V_{\rm max}(z = 1) < 7$ km/s is likely artificial, and caused by insufficient numerical resolution. Note that the z=0 subhalo velocity function of Via Lactea also starts to be affected by numerical limitations below the corresponding z=0 scale of about 5 km/s (Paper I).

One consequence of larger mass loss in larger systems is that subhalo mass and velocity functions should become steeper with time, especially near when a region approaches virialisation, since this is the time when most of the tidal mass loss happens (Section 3). Indeed, this trend can be observed in Figure 7. The mass range used in this Figure extends down to $V_{\rm max} = 5$ km/s, the trend is stronger when only large subhalos are considered: the

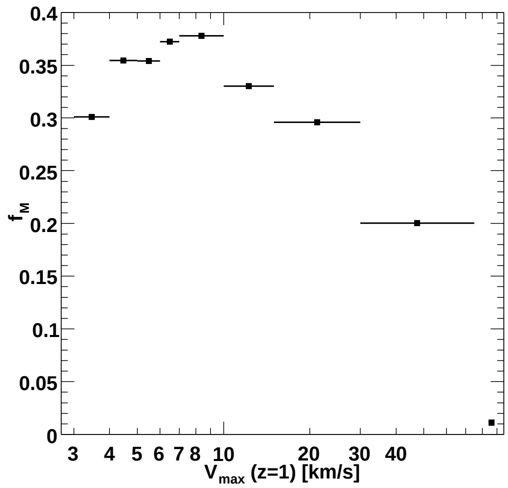

FIG. 18.— Retained mass fraction from $z = 1$ to $z = 0$ versus peak circular velocity range used to select the subhalos at $z = 1$. The largest subhalo is represented by the square at 86 km/s. Subhalos were selected at $z = 1$ within a sphere containing $M_{200} = 1.8 \times 10^{12}$ $M_\odot$. The largest subhalos are sinking towards the center due to dynamical friction, and they retain only a relatively small fraction of their initial mass. Smaller subhalos are on more stable orbits and lose less mass. The smallest systems (below about 7 km/s or 1000 particles at z=1) suffer from an artificially large mass loss caused by the finite numerical resolution.

slope of the cumulative velocity function of subhalos with $V_{\rm max} > 10$ km/s measured within shells 1-6 grows from 2.81 to 3.35 from $z \simeq 2$ to $z \simeq 1$, and remains roughly constant from then until $z = 0$.

5. SUMMARY AND CONCLUSIONS

We have analyzed the co-evolution of the Via Lactea host halo and its subhalo population. The simulation follows the formation of a Milky Way-size halo in a *WMAP* 3-year cosmology with 234 million DM particles. Here we summarize our main results:

- In agreement with Prada et al. (2006) we find that the formal virial radius, defined in terms of comoving scales, underestimates the actual virialized region of ΛCDM galaxy halos. The increase in M_{200} and $M_{\rm vir}$ after $z = 1$ is almost entirely due to apparent accretion, resulting from the artificial increase of the virial radius. Typically around 90% of the final M_{200} is already within the final r_{200} at $z = 1$. When halo mass is based on physical scales, such as $V_{\rm max}$ or mass within $r_{\rm Vmax}$, we find no evidence for a late epoch of quiescent mass accretion as advocated by recent studies (e.g. Wechsler et al. 2002; Zhao et al. 2003).

- The collapse factors of shells enclosing a fixed mass are very different from the factor of two found in the idealized top-hat collapse. This causes the shortcomings of $r_{\rm vir}$.

- The abundance of substructure co-evolves closely with the host halo. The subhalo mass loss rate peaks between the epochs of turnaround and stabilization and declines after a region has virialized. Mass and velocity functions become slightly steeper during this process.

- Tides remove subhalo mass from the outside in, which leads to higher concentrations compared to field halos of the same mass. This effect, combined with the earlier formation of inner subhalos, results in strongly increasing subhalo concentrations towards the host center.

- Selecting the earliest forming systems, or the largest before accretion, gives largely overlapping and at $z = 0$ nearly indistinguishable subhalo samples. They typically show large, early mass loss and high concentrations, especially those found near the Galactic center today.

- We confirm the result by Balogh et al. (2000); Moore et al. (2004); Gill et al. (2005) that many subhalos end up in the "field" (outside the virial radius) and quantify the environment dependence of halo formation times caused by this effect. Defining halo formation times relative to the maximum circular velocity a halo reaches over its lifetime removes the environment dependence of median formation times, but not the environment dependence of halo mass assembly histories. Due to the strongly nonlinear tidal origin of the effect, correcting analytic approximations seems difficult and simulations should be employed whenever structure formation needs to be followed accurately.

- At the first pericenter passage a larger average mass fraction is lost than during each one of the following orbits. The median peri- to apocenter ratio is close to 1:6 (as in Ghigna et al. 1998) and only 5 % of the subhalo orbits are rounder than 2:3.

- We find that 97% of all $z = 1$ subhalos have a surviving $z = 0$ remnant. The retained mass fraction is larger for subhalos with smaller initial mass. Satellites with $V_{\rm max} \simeq 10$ km/s retain about 40% of their $z = 1$ mass at the present epoch.

It is a pleasure to thank Joachim Stadel for making PKDGRAV available to us. We also like to thank the referee Andrew Zentner for a very detailed and helpful report and Avishai Dekel, Vincent Desjacques, Andreas Faltenbacher, Susan Kassin, Jason Kalirai, Andrey Kravtsov, Ben Moore, Francisco Prada, Miguel Angel Sanchez-Conde, Joachim Stadel, Simon White, and Marcel Zemp for useful discussions and/or comments on earlier drafts of this paper. J. D. acknowledges financial support from the Swiss National Science Foundation and from NASA through Hubble Fellowship grant HST-HF-01194.01 awarded by the Space Telescope Science Institute, which is operated by the Association of Universities for Research in Astronomy, Inc., for NASA, under contract NAS 5-26555. MK gratefully acknowledges support from the Institute for Advanced Study. P.M. acknowledges support from NASA grants NAG5-11513 and NNG04GK85G, and from the Alexander von Humboldt Foundation. All computations were performed on NASA's Project Columbia supercomputer system.

REFERENCES

Alam, S. M. K., Bullock, J. S., & Weinberg, D. H., 2002, ApJ, 572, 34
Balogh, M. L., Navarro, J. F., & Morris, S. L. 2000, ApJ, 540, 113
Bertschinger, E. 2001, ApJSS, 137, 1
Bryan, G. L., & Norman, M. L. 1998, ApJ, 495, 80
Bullock, J. S., et al. 2001, MNRAS, 321, 559
Bullock, J. S., Kravtsov, A. V., & Weinberg, D. H. 2000, ApJ, 539, 517
Cole S., Kaiser N., 1989, MNRAS, 237, 1127
Harker, G., Cole, S., Helly, J., Frenk, C., & Jenkins, A. 2006, MNRAS, 367, 1039
Hayashi, E., Navarro, J. F., Taylor, J. E., Stadel, J., & Quinn, T. 2003, ApJ, 584, 541
Dekel, A., Devor, J., & Hetzroni, G. 2003, MNRAS, 341, 326
Diemand, J., Moore, B., & Stadel, J. 2004, MNRAS, 352, 535
Diemand, J., Madau, P., & Moore, B. 2005, MNRAS, 364, 367
Diemand, J., Kuhlen, M., & Madau, P. 2006, ApJ, 649, 1
Diemand, J., Kuhlen, M., & Madau, P. 2007, ApJ, 657, 262 (Paper I)
Faltenbacher, A., Gottloeber, S., & Mathews, W. G. 2006, preprint (astro-ph/0609615)
Fukushige, T., Kawai, A., & Makino, J. 2004, ApJ, 606, 625
Gao, L., Springel, V., & White, S. D. M. 2005, MNRAS, 363, L66
Gao, L., White, S. D. M., Jenkins, A., Stoehr, F., & Springel, V. 2004, MNRAS, 355, 819
Ghigna, S., Moore, B., Governato, F., Lake, G., Quinn, T., & Stadel, J. 1998, MNRAS, 300, 146
Ghigna, S., Moore, B., Governato, F., Lake, G., Quinn, T., & Stadel, J. 2000, ApJ, 544, 616
Gill, S. P. D., Knebe, A., & Gibson, B. K. 2005, MNRAS, 356, 1327
Gnedin, O. Y., & Ostriker, J. P. 1997, ApJ, 474, 223
Governato, F., Willman, B., Mayer, L., Brooks, A., Stinson, G., Valenzuela, O., Wadsley, J., & Quinn, T. 2007, MNRAS, 374, 1479
Kassin, S., et al. 2007, ApJ, in press (astro-ph/0702643)
Kazantzidis, S., Mayer, L., Mastropietro, C., Diemand, J., Stadel, J.,& Moore B. 2004, ApJ, 608, 663
Kleyna, J. T., Wilkinson, M. I., Evans, N. W., & Gilmore, G. 2005, ApJ, 630, L141
Klypin, A., Kravtsov, A. V., Valenzuela, O., & Prada, F. 1999, ApJ, 522, 82
Koch, A., Wilkinson, M. I., Kleyna, J. T., Gilmore, G. F., Grebel, E. K., Mackey, A. D., Evans, N. W., & Wyse, R. F. G. 2007, ApJ, 657, 241
Kravtsov, A. V., Gnedin, O. Y., & Klypin, A. A. 2004, ApJ, 609, 482
Kuhlen, M., Strigari, L. E., Zentner, A. R., Bullock, J. S., & Primack, J. R. 2005, MNRAS, 357, 387
Łokas, E. L., Mamon, G. A., & Prada, F. 2005, MNRAS, 363, 918
Macciò, A. V., Murante, G., & Bonometto, S. P. 2003, ApJ, 588, 35
Maccio', A. V., Dutton, A. A., van den Bosch, F. C., Moore, B., Potter, D., & Stadel, J. 2006, preprint (astro-ph/0608157)
Mayer, L., Governato, F., Colpi, M., Moore, B., Quinn, T., Wadsley, J., Stadel, J., & Lake, G. 2001, ApJ, 547, L123
Mayer, L., Governato, F., Colpi, M., Moore, B., Quinn, T., Wadsley, J., Stadel, J., & Lake, G. 2001, ApJ, 559, 754
Mayer, L., Kazantzidis, S., Mastropietro, C., & Wadsley, J. 2007, Nature, 445, 738-740
Moore, B., Diemand, J., Madau, P., Zemp, M., & Stadel, J. 2006, MNRAS, 368, 563
Moore, B., Diemand, J., & Stadel, J. 2004, IAU Colloq. 195: Outskirts of Galaxy Clusters: Intense Life in the Suburbs, 513
Moore, B., Calcáneo-Roldán, C., Stadel, J., Quinn, T., Lake, G., Ghigna, S., & Governato, F. 2001, PRD, 64, 063508
Moore, B., Ghigna, S., Governato, F., Lake, G., Quinn, T., Stadel, J., & Tozzi, P. 1999, ApJ, 524, L19
Moore, B., Katz, N., & Lake, G. 1996, ApJ, 457, 455
Navarro, J. F., Frenk, C. S., & White, S. D. M. 1997, ApJ, 490, 493
Penarrubia, J., McConnachie, A., & Navarro, J. F. 2007, preprint (astro-ph/0701780)
Prada, F., Klypin, A. A., Simonneau, E., Betancort-Rijo, J., Patiri, S., Gottlöber, S., & Sanchez-Conde, M. A. 2006, ApJ, 645, 1001
Romano-Diaz, E., Faltenbacher, A., Jones, D., Heller, C., Hoffman, Y., & Shlosman, I. 2006, ApJ, 637, L93
Read, J. I., Wilkinson, M. I., Evans, N. W., Gilmore, G., & Kleyna, J. T. 2006, MNRAS, 366, 429
Reed, D., Governato, F., Quinn, T., Gardner, J., Stadel, J., & Lake, G. 2005, MNRAS, 359, 1537
Sanchez-Conde, M. A., Betancort-Rijo, J., & Prada, F. 2006, preprint (astro-ph/0609479)
Sheth, R. K., & Tormen, G. 1999, MNRAS, 308, 119
Sheth, R. K., & Tormen, G. 2004, MNRAS, 350, 1385
Spergel, D. N., et al. 2006, ApJ, submitted (astro-ph/0603449)
Stadel, J. 2001, PhD thesis, U. Washington
Strigari, L. E., Koushiappas, S. M., Bullock, J. S., & Kaplinghat, M. 2006, preprint (astro-ph/0611925)
Taffoni, G., Mayer, L., Colpi, M., & Governato, F. 2003, MNRAS, 341, 434
Taylor, J. E., & Babul, A. 2001, ApJ, 559, 716
van den Bosch, F. C., Tormen, G., & Giocoli, C. 2005, MNRAS, 359, 1029
Wang, H. Y., Mo, H. J., & Jing, Y. P. 2006, preprint (astro-ph/0608690)
Wechsler, R. H., Bullock, J. S., Primack, J. R., Kravtsov, A. V., & Dekel, A. 2002, ApJ, 568, 52
Weiner, B. J., et al. 2006, ApJ, 653, 1027
Zhao, D. H., Mo, H. J., Jing, Y. P., Börner, G. 2003, MNRAS, 339, 12
Zentner, A. R., & Bullock, J. S. 2003, ApJ, 598, 49
Zentner, A. R., Berlind, A. A., Bullock, J. S., Kravtsov, A. V., & Wechsler, R. H. 2005, ApJ, 624, 505